Electronic Seismologist

FDFK2D: Efficient Two-Dimensional Teleseismic Wavefield Modeling for Receiver Function Analysis Using a Hybrid Method

Youshan Liu*[1], Chenglong Wu[2], Tao Xu[2,3], Liang Zhao[1,3], and Jiwen Teng[1,3]

Abstract

We develop a Fortran package with high programming optimization and parallel computing for simulating high-frequency (> 1 Hz) teleseismic wavefields using a hybrid numerical method that couples the finite-difference (FD) and frequency–wavenumber (FK) methods. This method can simulate the interactions of incoming teleseismic wavefields with local heterogeneities but reduce computational region to a much smaller localized domain, which can significantly reduce the computing cost of the high-frequency teleseismic wavefields. The local heterogeneities are allowed to vary arbitrarily in a localized heterogeneous domain. In this package, the geographical locations of earthquakes are permitted, which can consider the real azimuthal effect of the source. Numerical benchmark tests first demonstrate the effectiveness of the developed method for *P*- and *S*-wave receiver functions (RFs). The consistent travel times of synthetic and theoretical RFs phases demonstrate its high accuracy. Application on a dense array generally obtains consistent RFs profiles with observed ones and successfully reproduces the observed common-converted-point (CCP) stacking image, which further verifies the effectiveness of the presented method. In addition, statistics of the time-consuming of typical models illustrate the high efficiency of this package, which needs very little computing resources even to be feasible on a laptop.

Cite this article as Liu, Y., C. Wu, T. Xu, L. Zhao, and J. Teng (2024). FDFK2D: Efficient Two-Dimensional Teleseismic Wavefield Modeling for Receiver Function Analysis Using a Hybrid Method, *Seismol. Res. Lett.* **96**, 1163–1180, doi: 10.1785/0220240231.

Introduction

Receiver function (RF) has been an indispensable tool for imaging the structures of Earth's interior (Langston, 1979; Ammon, 1991). The resultant images provide crucial evidence for the tectonic evolution and internal geodynamic processes of the Earth. RF has been applied routinely to study crustal and upper-mantle structures, such as basins, Moho, subduction zones, lithosphere–asthenosphere boundary (LAB), and mantle transition zones (Zhu and Kanamori, 2000; Chen *et al.*, 2009; Nábelek *et al.*, 2009; Fischer *et al.*, 2010; Zhong and Zhan, 2020). RF imaging relies mainly on teleseismic records for those regions with low seismicity. In regions with complex structures and thick sedimentary basins, RF image needs comprehensive synthetic experiments to verify the reliability of the results which requires a large number of numerical simulations of teleseismic wavefields (Zhao *et al.*, 2015). Because numerical simulations of seismic waves below the period of 8 s at globe scale are still computationally prohibitive (Komatitsch *et al.*, 2005), it is challenging to simulate high-frequency (>1 Hz) teleseismic wavefields recorded at stations from a distant seismic source by incorporating them in a unified model. Therefore, a hybrid method is usually adopted to simulate high-frequency teleseismic wave propagation in heterogeneous media. This approach couples a localized 2D or 3D numerical simulation solver with a fast and efficient analytical, semianalytical, or numerical 1D solution on the interfacing boundary, which can simulate seismic wave propagation in complex heterogeneous media while drastically reducing the computational demand (Robertsson *et al.*, 1996; Opršal *et al.*, 2002; Monteiller *et al.*, 2013, 2020; Tong, Chen, *et al.*, 2014; Tong,

1. State Key Laboratory of Lithospheric and Environmental Coevolution, Institute of Geology and Geophysics, Chinese Academy of Sciences, Beijing, China, https://orcid.org/0000-0003-3895-5008 (YL); https://orcid.org/0000-0002-0219-8722 (LZ); 2. Key Laboratory of Mineral Resources, Institute of Geology and Geophysics, Chinese Academy of Science, Beijing, China; 3. University of Chinese Academy of Sciences, Beijing, China

*Corresponding author: ysliu@mail.iggcas.ac.cn

Komatitsch, *et al.*, 2014). The assumption behind the hybrid method is that only 2D/3D effects inside the heterogeneous domain matter, whereas 2D/3D effects outside the domain are negligible, and only 1D incident wavefield of solution to either 1D layered model or 1D spherical earth model is computed (Tong, Chen, *et al.*, 2014; Tong, Komatitsch, *et al.*, 2014).

The idea behind the hybrid methods of seismic wavefield simulation can be traced back to the work of accurately dealing with the singularity of seismic sources (Alterman and Karal, 1968). Usually, the hybrid methods allow to compute seismic wavefields in elastic/anisotropic media containing a complex local structure embedded in a large, but considerably simpler, regional/global structure (Opršal *et al.*, 2002). These methods are implemented in two successive steps. In the first step, a fast and efficient analytical, semianalytical, or numerical method is adopted to calculate the wavefields excited by a distant source in a 1D background medium without localized geological structures, which contains the source and path effects. The time history of these incident wavefields is recorded at the boundary of an excitation box, which encloses a small portion of the computational domain with 2D/3D heterogeneities, to simulate responses of a reduced region with localized heterogeneities and large velocity contrasts to earthquake ground motion in the second step. Shtivelman (1984, 1985) first adopted this idea to develop a hybrid method for wavefield computation in 2D heterogeneous media by combining analytical and numerical techniques. Then, engineering seismologists developed a hybrid method by coupling the modal summation and the finite-difference (FD) method to simulate the response of buildings, basins, and soil–structure interactions to large earthquakes for hazard assessment (Bielak and Christiano, 1984; Fäh and Suhadolc, 1994; Fäh *et al.*, 1994; Bielak *et al.*, 2003). Subsequently, many variants of hybrid methods combining different methods were developed (Ma and Zhu, 2004; Ma *et al.*, 2004; Wang and Tian, 2005; Galis *et al.*, 2008).

A two-side (source and receiver sides) hybrid method by combining generalized ray theory (GRT) and the FD method to simulate strong ground motion (Wen and Yao, 1994, 1995) and to consider localized structures near the core-mantle boundary (Wen and Helmberger, 1998) was developed. Following the work of Wen and Helmberger (1998), Zhao *et al.* (2008, 2014) developed an FD–GRT hybrid method to calculate synthetic seismograms in 2D heterogeneous and anisotropic media. Robertsson *et al.* (1996) developed a hybrid method that couples a Gaussian beam method and the FD method to study the ocean acoustic problems, and compared with the Jeffreys-Wentzel-Kramers-Brillouin (JWKB) (Jeffreys, 1924; Wentzel, 1926; Kramers, 1926; Brillouin, 1926) approximation method and full FD simulation. Besides, the discrete-wavenumber (DW) method (Zahradník and Moczo, 1996) and pseudospectral (PS) method (Huang and Shih, 1997) coupling with the FD method were also developed, respectively. To deal with the free-surface topography, Moczo *et al.* (1997) presented a hybrid method based on a combination of the DW, FD, and finite-element method (FEM), in which the DW method was adopted to calculate wave propagation in the 1D background medium, whereas the FD–FEM algorithm was used to compute the wave propagation for inclusion of topography. In theory, Robertsson and Chapman (2000) summarized the principle of hybrid methods, they called the algorithm behind the hybrid methods as the wavefield injection technique. Inspired by this theoretical insight, the simulations of distant earthquake ground motion were also carried out by using 3D hybrid methods of FD–Ray, FD–DW, and FD–FEM (Opršal and Zahradnik, 2002; Opršal *et al.*, 2002, 2005; Yoshinmura *et al.*, 2003). For full waveform teleseismic tomography, Roecker *et al.* (2010) coupled a 2D spectral domain FD method with a plane-wave propagation through a 2.5D elastic medium. Recently, Ma *et al.* (2018) and Meng *et al.* (2021) developed a hybrid method by coupling the frequency–wavenumber (FK) and time–space-optimized symplectic method for numerically solving elastic wave equations in heterogeneous isotropic media.

Although the FD method is computationally efficient, it is difficult to apply to complex geological models with large free-surface or interface topography that is usually encountered in practice. To overcome this limitation, some more geometrically flexible method, such as the FEM or spectral element method (SEM), based hybrid methods were developed. In global Earth, Capdeville *et al.* (2003) presented a hybrid method that couples the SEM with a modal solution method, which decomposed the Earth into two parts, the outer shell with 3D lateral heterogeneities was solved by the SEM, whereas the inner sphere with only spherically symmetrical heterogeneities was solved by modal solution in frequency domain after expansion on the spherical harmonic basis (Capdeville *et al.*, 2003). Then, a hybrid method interfacing a 1D direct solution method (DSM) with the SEM to compute short-period teleseismic seismograms in 3D regional models with heterogeneities was developed (Chevrot *et al.*, 2011; Monteiller *et al.*, 2013, 2020). As the wavefronts of teleseismic waves beneath seismic arrays can be safely assumed to be planar (Rondenay, 2009; Tong, Chen, *et al.*, 2014; Tong, Komatitsch, *et al.*, 2014), analytical methods, such as FK method can be utilized to accurately and efficiently compute plane-wave responses of 1D medium (Zhu and Rivera, 2002). Thus, a hybrid method coupling the SEM with FK was developed to simulate high-frequency teleseismic wavefield effectively (Tong, Chen, *et al.*, 2014; Tong, Komatitsch, *et al.*, 2014; Xu *et al.*, 2024). Benefiting from the efficiency of the AxiSEM (Nissen-Meyer *et al.*, 2014), a hybrid method that combines the SEM (Komatitsch and Tromp, 1999) and AxiSEM was developed and applied in adjoint tomography (Beller *et al.*, 2018). Subsequently, Leng *et al.* (2016, 2019) developed a hybrid method called AxiSEM3D to simulate global wave propagation considering a 3D Earth model with

undulating discontinuities by combining the PS and SEM. Lately, he combined the SEM and AxiSEM3D to simulate 3D small-scale heterogeneities in Earth's mantle up to 1 Hz dominant frequency (Leng *et al.*, 2020). In addition, Ba *et al.* (2022) applied an SEM–FK hybrid method to simulate ground motion due to point dislocation sources. Wu *et al.* (2018) developed a source-side hybrid method by combining the DSM and SEM based on the representation theorem. Recently, Lyu *et al.* (2022) presented a review of the SEM-based hybrid methods.

As RF mainly uses teleseismic records from distant sources, a plane-wave approximation in FK is safe for seismic arrays with limited aperture. On the other hand, RF analysis may involve hundreds of teleseismic wavefield simulations to obtain a reliable migration velocity model (Zhao *et al.*, 2015), an FD–FK hybrid method is especially appealing for RF analysis due to its high efficiency. In this study, given the high efficiency of the FD and FK methods, we develop an efficient open-source software package using the FD–FK hybrid method to calculate the synthetic response of local heterogeneous media to teleseismic plane-wave incidence, especially for RFs analysis. We first review the theory and deduction of the FK method. Theoretically, we prove the nonuniqueness and intrinsic relations of the propagation matrix. Then, we present the implementation details and efficient computing strategy for the FD–FK hybrid method using a unified wavefield variable and discuss its storage

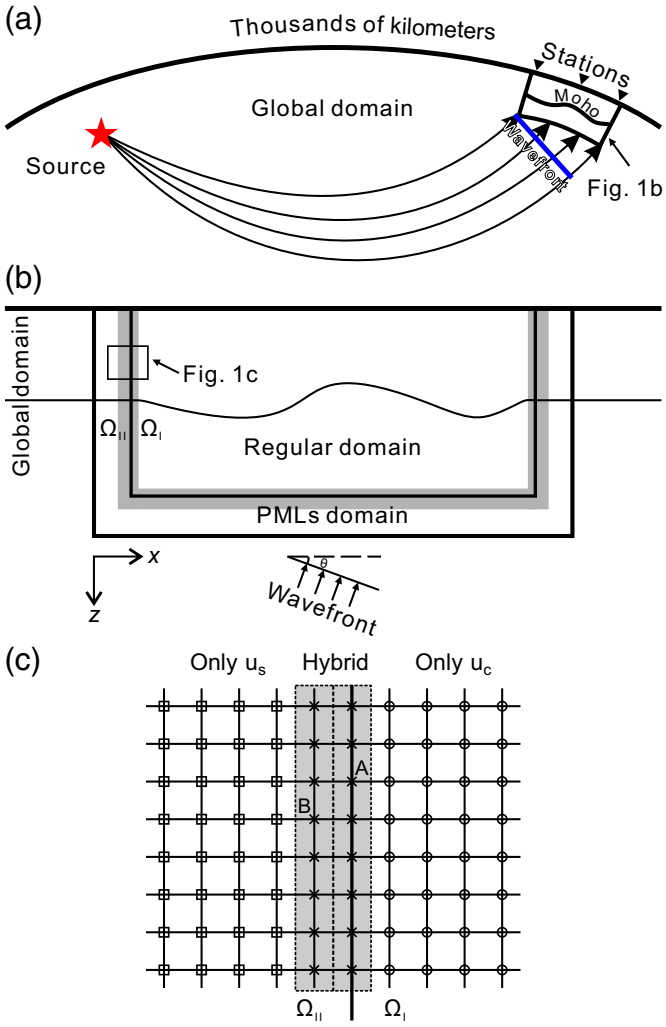

Figure 1. Schematic diagram of teleseismic wavefield simulation using a hybrid method. (a) The geometry of stations (black inverted triangles) with an aperture of a few hundred kilometers recording teleseismic wavefields from a few thousand of kilometers distant source (red pentagram). The domain can be divided into two parts, that is, a 1D global domain and a 3D heterogeneous domain (box in the top-right corner). A fast and efficient method (such as frequency–wavenumber [FK], direct solution method [DSM], and AxiSEM, etc.) is adopted to obtain solution in 1D media, whereas numerical method (such as finite-difference [FD] method, finite-element method [FEM], and spectral element method [SEM], etc.) being capable of simulating 3D heterogeneous media is adopted in the local region shown in the box at the top-right corner. The enlarged view of a reduced region with localized heterogeneities is shown in panel (b). (b) The local region is used to simulate responses of a reduced region with localized heterogeneities and large velocity contrasts to earthquake ground motion. In the region inside the outer rectangle, the regions are divided into regular (Ω_I) and perfectly matched layers (PMLs) (Ω_{II}) domains, and the PMLs boundary conditions are applied to the latter to attenuate spurious reflections from the artificial truncated boundary. The region outside the inner rectangle is the global domain in which a fast and efficient 1D wavefield simulation method is applied to obtain background wavefield $\mathbf{u}_0$, whereas a numerical method is adopted inside this rectangle to adapt to heterogeneities. Wavefields computed by these two methods are coupled/interacted near this boundary (the gray zones). The wavefield coupling or wavefield injection technique is shown in panel (c). (c) Principle of wavefield injection technique on the left boundary. The black thick line denotes the boundary between the regular and PMLs domains, and the black-dashed line represents the symmetry axis of the coupling region (gray zone). In the right domain of the gray zone, only the complete wavefield $\mathbf{u}_c$ (denoted by open circles) is involved, whereas only the scattered wavefield $\mathbf{u}_s$ (denoted by open squares) is involved in the left domain of the gray zone. In this gray zone, both the scattered wavefield $\mathbf{u}_s$ and complete wavefield $\mathbf{u}_c$ are involved, that is the hybrid wavefield (denoted by crosses). The 1D media on the left and right are used for waves entering from the left and right, respectively, and are not necessarily the same. The color version of this figure is available only in the electronic edition.

demand and countermeasures. Subsequently, we conduct five benchmark tests to verify the accuracy and effectiveness of the presented method for RFs analysis. Finally, an application to short-period dense array experiment is implemented to further demonstrate the promising capabilities of the method. In addition, statistics of computing time are shown to illustrate its high efficiency.

Method

RF extracts structural information beneath stations by deconvoluting the vertical component from the radial component, which uses teleseismic records with large epicentral distance (30°–90°) and high frequency (~1 s or higher especially for short-period array). It is impractical to simulate such high-frequency teleseismic wavefields at a global scale or even regional scale a large number of times. To reduce the computational cost, hybrid methods were developed to simulate high-frequency teleseismic wavefields. As shown in Figure 1, hybrid methods adopt different methods to simulate the seismic propagation in the 1D background and 3D heterogeneous media sharing the same model at coupling boundary/zone. Usually, hybrid methods first adopt fast and efficient analytical, semianalytical, or numerical methods, such as the normal modes, GRT, DWM, FK, DSM, and AxiSEM, and so forth, to compute the seismic wavefields $\mathbf{u}_0$ propagating in 1D background medium (i.e., the global domain in Fig. 1a or layered model in Fig. 1b) from a distant seismic source (typically thousands of kilometers). Then the complete/full wavefields $\mathbf{u}_c$ in 3D heterogeneous media (inside the inner rectangle in Fig. 1b) are simulated using the FD, FEM, SEM, and so forth, in which the wavefield injection boundary condition is applied simultaneously to couple with the 1D solution at the interfacing boundary/zone (Fig. 1b,c). These two processes share the identical structure at this interface boundary/zone (gray zone in Fig. 1b, c), whereas the structure inside the heterogeneous domain (inner rectangle in Fig. 1b) can be arbitrarily different from the 1D Earth model. In addition, although the 1D media on the left and right sides are schematically identical as shown in Figure 1c, they are not necessarily the same.

FK method

FK is one of the efficient methods of simulating seismic wavefields in a 1D medium, which synthesizes the seismograms of plane waves traveling through a layered model using the propagator matrix between layers (Thomson, 1950; Haskell, 1953, 1962; Zhu *et al.*, 2002). As the teleseismic records used by RF analysis are usually from distant seismic sources, it is safe to assume the wavefronts of teleseismic body waves to be planar when arriving in the upper mantle beneath a seismic array with a limited aperture (Tong, Chen, *et al.*, 2014). As shown in Figure A1, for an n-layer layered model, the displacement–stress response of an incident plane wave to the n + 1th layer, that is, the bottom half-space layer, at a reference point (x_o,y_o,z_o) can be written

$$\mathbf{y}_{z=z_0}=\mathbf{P}_1\mathbf{P}_2\cdots\mathbf{P}_n\mathbf{R}_{n+1}\mathbf{H}(z_n-z_o)\begin{bmatrix}D_S\\U_S\\D_P\\U_P\end{bmatrix}\mathrm{e}^{-ik_h[(x-x_o)\cos\phi+(y-y_o)\sin\phi]}, \tag{1}$$

considering downward z-axis (Fig. A1), the coefficients D_S, U_S, D_P, and U_P are amplitudes of the downgoing S wave, upgoing S wave, downgoing P wave, and upgoing P wave, respectively, which are unknown coefficients that can be uniquely determined using free-surface boundary condition and unit amplitude of incident waves (Tong, Chen, *et al.*, 2014), thus we can compute the wavefields on the surface using formula (1); $\mathbf{y}$ is the state vector, that is, displacement and stress components; $\mathbf{P}$ is the propagation matrix that is nonunique (see details in Appendix A). The detailed definitions of matrices $\mathbf{H}$, $\mathbf{R}$, and the algorithm of the FK method are presented in Appendix A.

As shown in Figure 1b,c, we need background wavefields $\mathbf{u}_0$ on the surface and in the underground. To compute the wavefield at arbitrarily location beneath surface, such as located at (x_r, y_r, z_r) in ith layer, we use the following recursive relationship:

$$\mathbf{y}_{z=z_r}=\mathbf{R}_i\mathbf{H}(z_r-z_{i-1})\mathbf{R}_i^{-1}\mathbf{P}_{i-1}^{-1}\cdots\mathbf{P}_2^{-1}\mathbf{P}_1^{-1}\mathbf{y}_{z=z_0}. \tag{2}$$

This is the downward continuation process of wavefields on the surface. To improve the efficiency of the FK method, we first compute the propagation matrix from the bottom half-space layer to surface (Fig. A1) as the propagation matrices for all grids on the surface are identical except for the exponential phase shift factor in equation (1), then we compute downward continuation wavefields at each horizontal slice for a fixed z coordinate. After computing wavefield values at all frequencies and nodes, the frequency-domain Green's function is available. Then, it is multiplied by a source time function in frequency domain. As a result, the time-domain wavefields at coupling region (gray domain in Fig. 1c) can be obtained by inverse Fourier transform.

FD method

As we aim at developing an efficient 2D wavefield modeling method to simulate teleseismic wavefield, the following wave equations in 2D isotropic media are solved:

$$\begin{cases}\rho\frac{\partial^2 u_x}{\partial t^2}=\frac{\partial}{\partial x}\left[(\lambda+2\mu)\frac{\partial u_x}{\partial x}+\lambda\frac{\partial u_z}{\partial z}\right]+\frac{\partial}{\partial z}\left[\mu\left(\frac{\partial u_z}{\partial x}+\frac{\partial u_x}{\partial z}\right)\right]\\ \rho\frac{\partial^2 u_z}{\partial t^2}=\frac{\partial}{\partial x}\left[\mu\left(\frac{\partial u_z}{\partial x}+\frac{\partial u_x}{\partial z}\right)\right]+\frac{\partial}{\partial z}\left[\lambda\frac{\partial u_x}{\partial x}+(\lambda+2\mu)\frac{\partial u_z}{\partial z}\right]\end{cases}. \tag{3}$$

In this study, we use arbitrary higher-order FD method to solve the equations (3) by discretizing the time and space coordinates with $t=t_0+(n-1)\Delta t$, $x=x_0+(i-1)\Delta x$, $z=z_0+(j-1)\Delta z$, in which t_0 is the origin of time; (x_0, z_0) is the origin of space coordinates; n, i, j are the time and space grid indexes, respectively. All wavefield variables and material parameters are defined at regular grid nodes (Fig. A2). In FD scheme, the derivatives are approximated

by FDs (Alterman and Karal, 1968; Alford *et al.*, 1974; Kelly *et al.*, 1976; Dablain, 1986). For equations (3), the eight second-order spatial derivatives on the right can be generalized to the following two classes of specific FD approximations:

$$\frac{\partial}{\partial x}\left[M\frac{\partial u_{i,j}^{n}}{\partial x}\right]\approx\sum_{k=1}^{N}c_{k}^{N}\frac{M_{i+k-1/2,j}\frac{\partial u_{i+k-1/2,j}^{n}}{\partial x}-M_{i-k+1/2,j}\frac{\partial u_{i-k+1/2,j}^{n}}{\partial x}}{\Delta x}, \quad (4a)$$

$$\frac{\partial}{\partial x}\left[M\frac{\partial u_{i,j}^{n}}{\partial z}\right]\approx\sum_{k=1}^{N}d_{k}^{N}\frac{M_{i+k,j}\frac{\partial u_{i+k,j}^{n}}{\partial z}-M_{i-k,j}\frac{\partial u_{i-k,j}^{n}}{\partial z}}{2\Delta x}, \quad (4b)$$

in which M denotes the elastic moduli, that is, $\lambda+2\mu$, λ, or μ; u denotes displacement, that is, u_x or u_z; c_j^N and d_j^N are the jth $2N$-order FD coefficients corresponding to grid spacings of Δx and $2\Delta x$ (Dablain, 1986), respectively. The discretization of the first-order derivatives at integer and half-integer grids are listed in Appendix B. All other terms in equations (3) can be discretized by alternating the order of coordinate and displacement variables. Using the boundary conditions of strain discontinuity and stress continuity at interface, we can approximate the material parameters not at regular grid nodes (Moczo *et al.*, 2002). This scheme can adapt the FD method to deal with the heterogeneous media to weaken the scattered waves caused by staircase approximation. For the temporal derivative, we approximate it using the following second-order leapfrog format:

$$\frac{\partial^2 u_{i,j}^{n}}{\partial t^2}\approx\frac{u_{i,j}^{n+1}-2u_{i,j}^{n}+u_{i,j}^{n-1}}{\Delta t^2}. \quad (5)$$

Substituting equations (4) and (5) into equations (3), we can obtain a full discretizational forms of wave equations. To suppress spurious reflection waves from artificial truncated boundaries, we apply the perfectly matched layers (PMLs) boundary condition to the left, right, and bottom boundaries (Liu *et al.*, 2013, 2014). On the top boundary, we adopt the boundary-modified difference approximation to deal with the free-surface boundary condition (see details in Nilsson *et al.*, 2007; Lan and Zhang, 2011).

FD–FK hybrid method

To demonstrate the implementation of the FD–FK hybrid method, we take the left coupling boundary of Figure 1b as an example (shown in Fig. 1c). Here, we only show FD discretization with second-order precision for illustration, it is straightforward to extend to higher order precision. As shown in Figure 1c, the black thick line denotes the boundary between the regular domain (denoted by Ω_{I}) and PMLs domain (denoted by Ω_{II}); a coupling domain (gray zone) exists between them. This coupling domain involves both the scattered $\mathbf{u}_{\mathrm{s}}$ and complete/full $\mathbf{u}_{\mathrm{c}}$ wavefields (denoted by crosses), the width for which depends on the order of the FD operator, that is, half-length of the FD stencil. In this coupling domain, the black-dashed line separates it into two subdomains. In the region to the left of this black-dashed line, only the scattered wavefield is computed (denoted by squares), whereas only the complete wavefield is computed in the region to the right of this black dashed line (denoted by circles). Consequently, the wavefields in both domains can be generalized as the following unified wavefield variable:

$$\mathrm{u}_{hy}=\begin{cases}\mathrm{u}_{c}, & \text{in } \Omega_{\mathrm{I}}\\ \mathrm{u}_{s}, & \text{in } \Omega_{\mathrm{II}}\end{cases}, \quad (6)$$

in which $\mathbf{u}_{\mathrm{s}}=\mathbf{u}_{\mathrm{c}}-\mathbf{u}_{0}$ is the interactions of plane waves in the 1D background domain with the 2D heterogeneities in the regular domain; $\mathbf{u}_0$ is the wavefield in 1D background media obtained by the FK, whereas $\mathbf{u}_{\mathrm{c}}$ is the wavefield in 2D heterogeneous media obtained by the FD in this study. Generally, we solve this hybrid wavefield $\mathbf{u}_{\mathrm{hy}}$ in both domains obeying the wave governing equations (3). Therefore, the complete/full wavefield $\mathbf{u}_{\mathrm{c}}$ is solved in the regular domain, whereas the scattered wavefields $\mathbf{u}_{\mathrm{s}}$ is solved in the PMLs domain.

To illustrate the wavefield injection technique behind hybrid methods, we take two typical classes of nodes for demonstration. For the derivative in formula (4a), the discretization of the second-order derivative in the regular domain (node A in Fig. 1c) can be written as

$$\begin{aligned}\frac{\partial}{\partial x}\left[M\frac{\partial u_{c_{i,j}}^{n}}{\partial x}\right]_{\mathrm{A}}&\approx\frac{M_{i+1/2,j}(u_{c_{i+1,j}}^{n}-u_{c_{i,j}}^{n})-M_{i-1/2,j}(u_{c_{i,j}}^{n}-u_{c_{i-1,j}}^{n})}{\Delta x^2}\\&\approx\frac{M_{i+1/2,j}(u_{\mathrm{hy}_{i+1,j}}^{n}-u_{\mathrm{hy}_{i,j}}^{n})-M_{i-1/2,j}(u_{\mathrm{hy}_{i,j}}^{n}-u_{\mathrm{hy}_{i-1,j}}^{n})+M_{i-1/2,j}u_{0_{i-1,j}}^{n}}{\Delta x^2},\end{aligned} \quad (7a)$$

while its discretization in the PMLs domain (node B in Fig. 1c) can be written as

$$\begin{aligned}\frac{\partial}{\partial x}\left[M\frac{\partial u_{s_{i,j}}^{n}}{\partial x}\right]_{\mathrm{B}}&\approx\frac{M_{i+1/2,j}(u_{s_{i+1,j}}^{n}-u_{s_{i,j}}^{n})-M_{i-1/2,j}(u_{s_{i,j}}^{n}-u_{s_{i-1,j}}^{n})}{\Delta x^2}\\&\approx\frac{M_{i+1/2,j}(u_{\mathrm{hy}_{i+1,j}}^{n}-u_{\mathrm{hy}_{i,j}}^{n})-M_{i-1/2,j}(u_{\mathrm{hy}_{i,j}}^{n}-u_{\mathrm{hy}_{i-1,j}}^{n})-M_{i+1/2,j}u_{0_{i+1,j}}^{n}}{\Delta x^2}.\end{aligned} \quad (7b)$$

Compared with the standard second-order FD discretization of second-order derivative, there is an extra term ($+M_{i-1/2,j}u_{0_{i-1,j}}^{n}$ and $-M_{i+1/2,j}u_{0_{i+1,j}}^{n}$) in formulas (7a) and (7b) respectively, which can be considered as equivalent sources (van Manen *et al.*, 2020). Actually, this is an implementation of boundary integral in FD form. Naturally, it is straightforward to extend to other derivatives and boundaries/zones. In general, the background wavefield $\mathbf{u}_0$ should be added to the scattered wavefield values in the PMLs domain when used to compute derivatives at nodes in the regular domain, whereas it should be

subtracted from the complete wavefield values in the regular domain when used to compute derivatives at nodes in PMLs domain. Hence, the background wavefield $\mathbf{u}_0$, the scattered wavefield $\mathbf{u}_s$, and the complete wavefield $\mathbf{u}_c$ are simultaneously involved in the hybrid domain (i.e., the gray zone). However, either only $\mathbf{u}_s$ or only $\mathbf{u}_c$ is respectively involved in the two domains excluding the hybrid domain (i.e., the regular or PMLs domains outside the gray zones), which does not involve background wavefield computed by the FK method in 1D media. As a result, it needs to store background wavefield values $\mathbf{u}_0$ at nodes in a region (gray zones) with the width of half-length of FD stencil to implement the wavefield injection boundary condition behind the hybrid method of coupling the FD and FK for teleseismic wavefield modeling. Alternatively, an asymmetric FD operator can reduce the storage amount from this region to the boundary between the regular and PMLs domains like that done in Liu *et al.* (2015). By contrast, for those integration-based methods, such as the FEM and SEM, and so forth, the stored wavefield values are naturally reduced to the boundary between regular and PMLs domains as the propagation operator is elementwise global, thus only the displacement components on this boundary are needed to be stored (Liu *et al.*, 2017, 2019).

Numerical Examples

Five numerical experiments are conducted to verify the effectiveness and accuracy of the developed FD–FK hybrid method. In all experiments, the source time function is a Ricker wavelet with a dominant frequency of $f_0 = 1.0$ Hz, that is, with a cutoff frequency of about $3f_0 = 3.0$ Hz. The initial plane wavefront of FK is initialized on the vertical axis of symmetry of the profile with the depth depending on the incidence angle, that is, $z_o = z_n + \frac{L}{2}\tan\theta$, in which L= 200 km is the length of the profile and z_n is the maximum depth of the model. The model is discretized by square grids with intervals of 0.2 km in both horizontal and vertical directions. In wavefield simulation, the time sampling interval is 10 ms. Although the sixth-order FD is used and it can accurately simulate wavefield in 2D localized heterogeneous media, it is allowed to be set to any even order in the package. The geographical coordinates corresponding to the origin of the profile (x_0, z_0) are located at (45° N, 0° E), and the receivers are deployed along a linear array with azimuth of 0°. The source is located at (42° S, 10° E) and a depth of 50 km with the back-azimuth angle between locations of (x_0, z_0) and source being about 172.8°. The ray parameters of *P* and *S* waves are 4.798 and 9.535 s/°, respectively, which are computed by the *TauP* software (Crotwell *et al.*, 1999). The above parameters are used in the following experiments unless otherwise noted.

Benchmark tests

First, we conduct two benchmark tests to verify the precision of the developed hybrid method. As the FD method cannot deal with the subsurface accurately (Roecker *et al.*, 2010), we simulate the teleseismic wavefield in half-space for benchmark tests. The density, V_P, and V_S of the model are 2700 kg/m^3, 6000 m/s, and 3450 m/s, respectively. In this test, the duration of wavefield simulation is 40 s and the depth of the model is extended to 50 km. For this model, the solutions obtained by the FK and FD–FK hybrid methods are theoretically identical as the models used in both methods are the same. Therefore, the residuals between them can be used to evaluate the precision of the hybrid method. A receiver is deployed at (50 and 0 km) to record teleseismic wavefield for analysis. As shown in Figure 2, the waveforms obtained by the hybrid method are consistent with those obtained by the FK for both *P*- (Fig. 2a,b) and *S*-wave (Fig. 2c,d) incidences. The corresponding residuals are only a few percentage errors (~2% and 4% errors for *P*- and *S*-wave incidences, respectively), which illustrates the effectiveness and accuracy of the developed hybrid method.

To further demonstrate the effectiveness of the hybrid method, we simulate teleseismic wavefield and compute RFs in a single layer over a half-space model for both incident *P* and *S* waves. The parameters of this model are listed in Table 1. The duration of wavefield simulation is 45 s and the depth of the model is extended to 50 km. For *P*-wave incidence, the waveforms (Fig. 3a,c) and RF (Fig. 3d) at a receiver (50 and 0 km) are computed, and various phases are identified ray paths which are shown in Figure 3b. The snapshots of the horizontal displacement component computed by the FD–FK hybrid method at different time instants for *P*-wave incidence are shown in Figure A3. It can be observed that the direct *P* wave, transmitted *Pp* and *Ps* phases, *PpPp*, *PsPp*, *PsPs* multiples, and reflected *PP*, *PS* phases at the Moho interface. Figure 4 shows the waveforms (Fig. 4a,c), RF (Fig. 4d), and corresponding ray paths (Fig. 4b) for *S*-wave incidence. Since the *Sp* wave arrives earlier than the *Ss* wave, the phase of *Sp* (Fig. 4d) is on the negative half-axis in RF, whereas multiples *SpPp*, *SpPs*, *SsPs*, and *SpPpPs* are on the positive half-axis. Generally, as shown in Figures 3d and 4c, the travel times of phases are identical to the theoretical ones (vertical dashed lines), which further confirm the effectiveness of the hybrid method.

An LAB model

As the *S*-wave RF does not suffer from the interference by multiples at Moho, it is widely used to study the structure of LAB (Farra and Vinnik, 2000; Yuan *et al.*, 2006; Chen *et al.*, 2014; Mark *et al.*, 2021). To demonstrate that our method can be used in the study of LAB, we simulate the teleseismic wavefields of incident *S* wave and compute corresponding RFs in an LAB model. This model consists of two layers overlaying on a half-space layer, parameters for which are listed in Table 2. The duration of wavefield simulation is 60 s and the depth of the model is extended to 120 km. When a plane *S* wave is incident on the bottom of this model, seismograms of various phases (Fig. 5a,c) are recorded by a receiver at (50 and 0 km). As shown in Figure 5, the converted phases S_Lp at LAB and S_mp at the

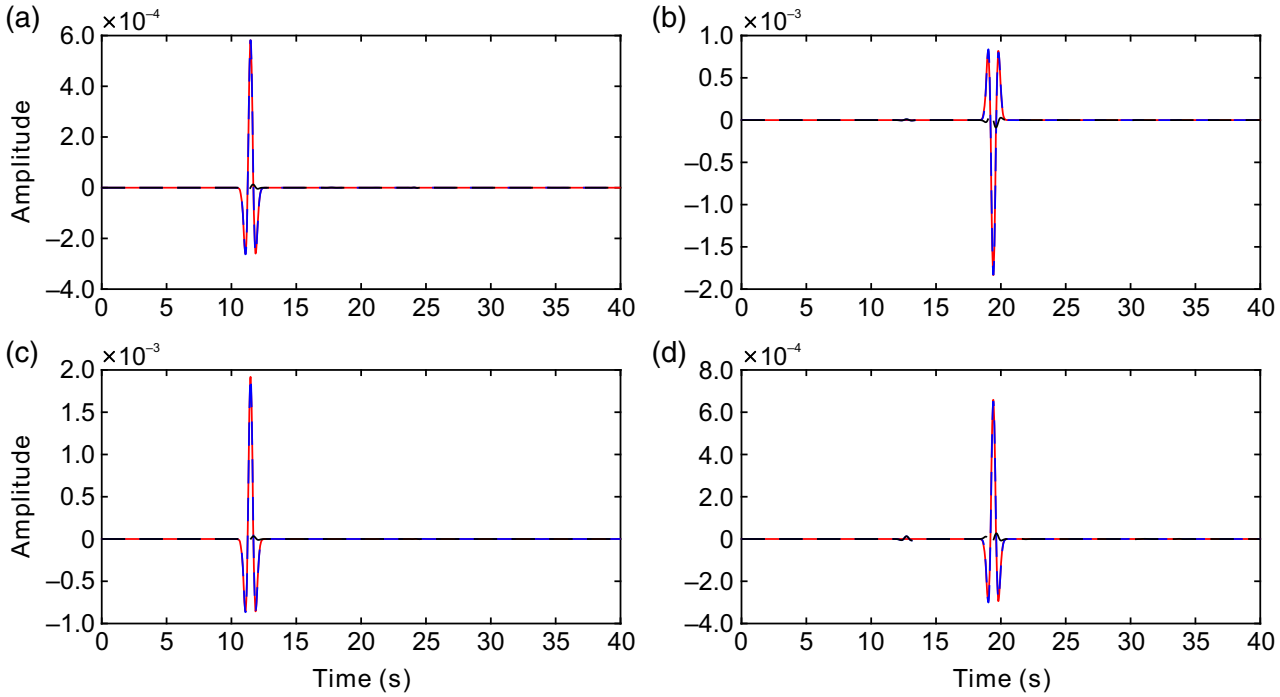

Figure 2. Benchmark tests for *P*- and *S*-wave incidence in a half-space model. Radial and vertical displacement components for (a,c) incident *P* wave recorded by a receiver at (50 and 0 km), and (b,d) incident *S* wave, respectively. The red lines denote solutions computed by the FK method, and the blue lines denote the solutions computed by the FD–FK hybrid method. The black lines denote corresponding residuals. The color version of this figure is available only in the electronic edition.

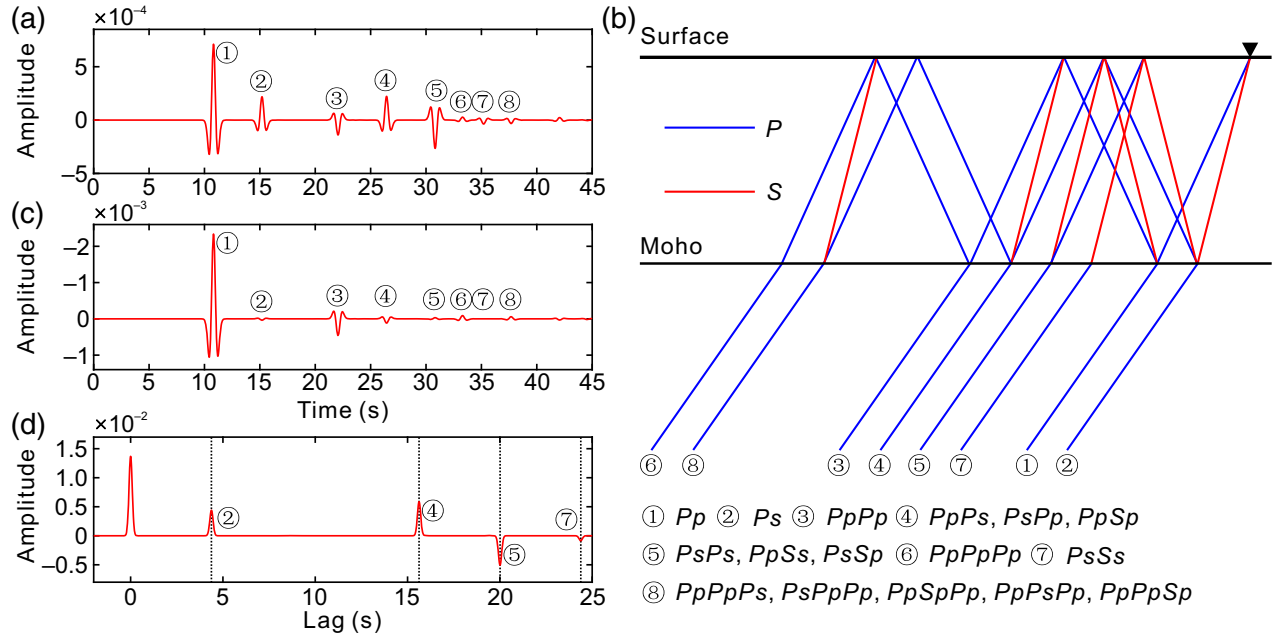

Figure 3. Displacement components, receiver function (RF), and corresponding ray paths of incident *P* wave in a single-layer overlaying half-space model. (a,c) Radial and vertical displacement components were computed by the FD–FK hybrid method and recorded by a receiver at (50 and 0 km), respectively. Ray paths corresponding to numbers in circles are shown in panel (b). (b) The corresponding *P*-wave RF. The vertical dotted lines are the theoretical travel times of corresponding phases. (d) Ray paths of various phases, in which blue and red lines represent *P*- and *S*-wave lags, respectively. The color version of this figure is available only in the electronic edition.

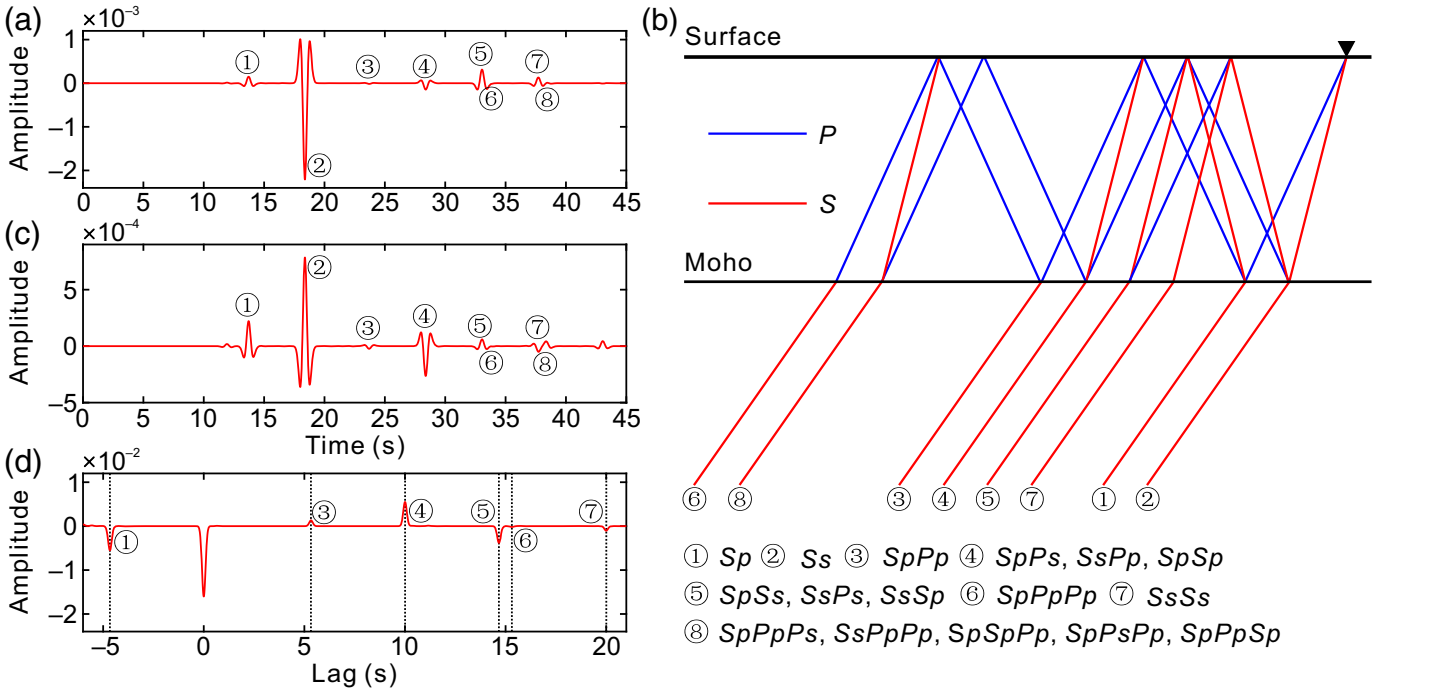

Figure 4. Displacement components, receiver function (RF), and corresponding ray paths of incident *S*-wave in a single-layer overlaying half-space model. (a,c) Radial and vertical displacement components computed by FD-FK hybrid method and recorded by a receiver at (50 km, 0 km), respectively. Ray paths corresponding to numbers in circles are shown in (b). (d) The corresponding original *S*-wave RF. The vertical dotted lines are the theoretical traveltimes of corresponding phases. (b) Ray paths of various phases, where blue and red lines represent *P*- and *S*-wave legs, respectively. The color version of this figure is available only in the electronic edition.

Moho boundary are on the negative half-axis in RF, whereas the multiples *SpPp*, *SpPs*, *SsPs*, and *SpPpPs* at the Moho boundary are on the positive half-axis. The ray paths of various phases are identified (Fig. 5b), and their theoretical travel times (vertical dotted lines) are consistent with corresponding RFs (Fig. 5d). It illustrates the effectiveness and feasibility of the presented hybrid method in the study of LAB structure.

Application

In this section, we apply the developed hybrid method to RFs analysis of real data acquired by a dense seismic array across the northern boundary of the Tibetan plateau. This array is generally running northwest–southeast trending with an azimuth of 134°, which consists of 483 short-period seismic stations along an ~380 km cross-section with an ~0.8 km station spacing (Fig. 6). The details on data and tectonic settings can be found in Wu *et al.* (2024). By incorporating existing data, Wu *et al.* (2024) constructed an optimal velocity model that best fits the real RFs (Fig. 7) after many tests. In general, this model consists of five layers overlaying on a half-space layer, that is, the sedimentary layers, upper and lower crust over the upper mantle, respectively. As the hybrid method requires that the 1D layered model used in FK must match the 2D heterogeneous model used in FD on coupling boundaries, the depth, density, and velocity values of each layer in both models should be identical on these boundaries. For this model, the depths of 1D background models on the left and right sides are set to be different to adapt to the 2D heterogeneous model as shown in Figure 7. As a result, the model in FK is a five-layer 1D model on both sides, whereas the model in FD (Fig. 7) is highly heterogeneous and complex. The detailed parameters of the 1D models on the left and right sides are listed in Table 3. Although these two models (i.e., models

TABLE 1
1D Single-Layer Model

Layers	V_P (m/s)	V_S (m/s)	Density (kg/m³)	Thickness (km)
Crust	6000.0	3450.0	2700.0	35.0
Half-space	8000.0	4450.0	3300.0	–

TABLE 2
1D Lithosphere–Asthenosphere Boundary (LAB) Model

Layers	V_P (m/s)	V_S (m/s)	Density (kg/m³)	Thickness (km)
Crust	6000.0	3450.0	2700.0	30.0
Mantle	8000.0	4450.0	3300.0	70.0
Half-space	7200.0	4000.0	3200.0	–

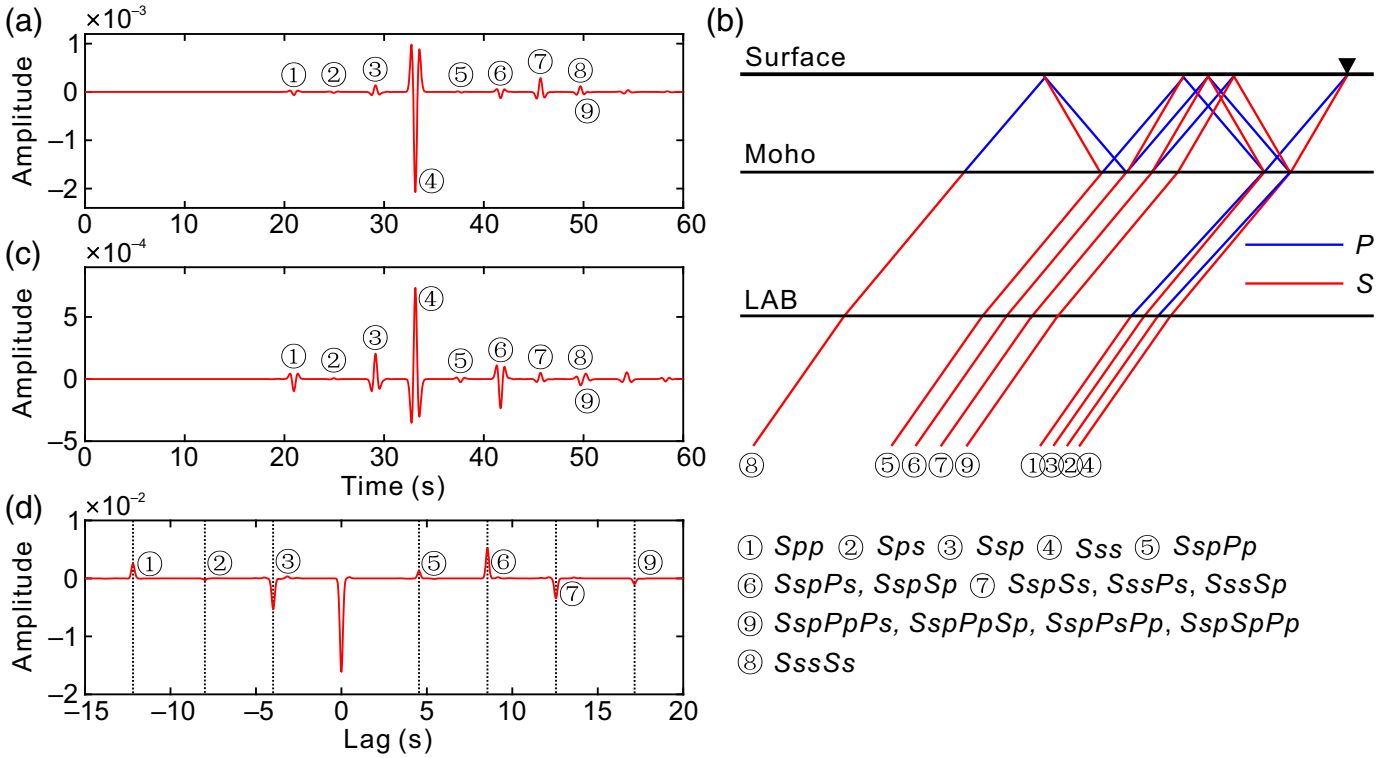

used in FK and FD) are significantly different in the region farther from the boundary, the hybrid method can effectively simulate the interactions of an incident plane wave with the heterogeneities in this reduced 2D localized region.

To further investigate the effectiveness and feasibility of the hybrid method for RFs analysis of real data, we show an application to a distant event located at (0.045° S, 124.28° E) at a depth of 39.85 km for demonstration (top-left inset in Fig. 6). The angle difference between the back-azimuth angle of this event and the azimuth of the profile is about 1.9°, which provides a perfect 2D geometry to compare the observed and synthetic RFs for a 2D wavefield modeling

Figure 5. Displacement components and receiver function (RF) of incident *S*-wave in a lithosphere–asthenosphere boundary (LAB) model. (a,c) The radial and vertical displacement components were computed by the FD–FK hybrid method and recorded by a receiver at (50 and 0 km). (d) The corresponding original *S*-wave RF. The vertical dotted lines are the theoretical travel times of corresponding phases. Phases S_Lp and S_mp are converted waves, respectively, at LAB and Moho boundaries, and phases S_mpP_mp, S_mpP_ms, S_mpS_ms, and $S_mpP_mpP_ms$ are multiples at the Moho interface, respectively. (b) Ray paths of various phases and blue and red lines represent *P*- and *S*-wave lags, respectively. The color version of this figure is available only in the electronic edition.

TABLE 3
Two 1D Models for the Dense Array Across Altyn Tagh Range

	Left				Right			
Layer Number	**V_P (m/s)**	**V_S (m/s)**	**Density (kg/m³)**	**Thickness (km)**	**V_P (m/s)**	**V_S (m/s)**	**Density (kg/m³)**	**Thickness (km)**
1	4700.0	2554.0	2058.0	3.0	4973.0	2810.0	2157.0	0.8
2	5200.0	2826.0	2239.0	3.0	5473.0	3092.0	2338.0	1.0
3	5600.0	3043.0	2384.0	2.8	5782.0	2067.0	2450.0	1.0
4	6300.0	3424.0	2638.0	19.4	6209.0	3508.0	2605.0	26.6
5	7000.0	3804.0	2891.0	23.6	6727.0	3800.0	2792.0	24.8
Half-space	8200.0	4633.0	3326.0	–	8200.0	4633.0	3326.0	–

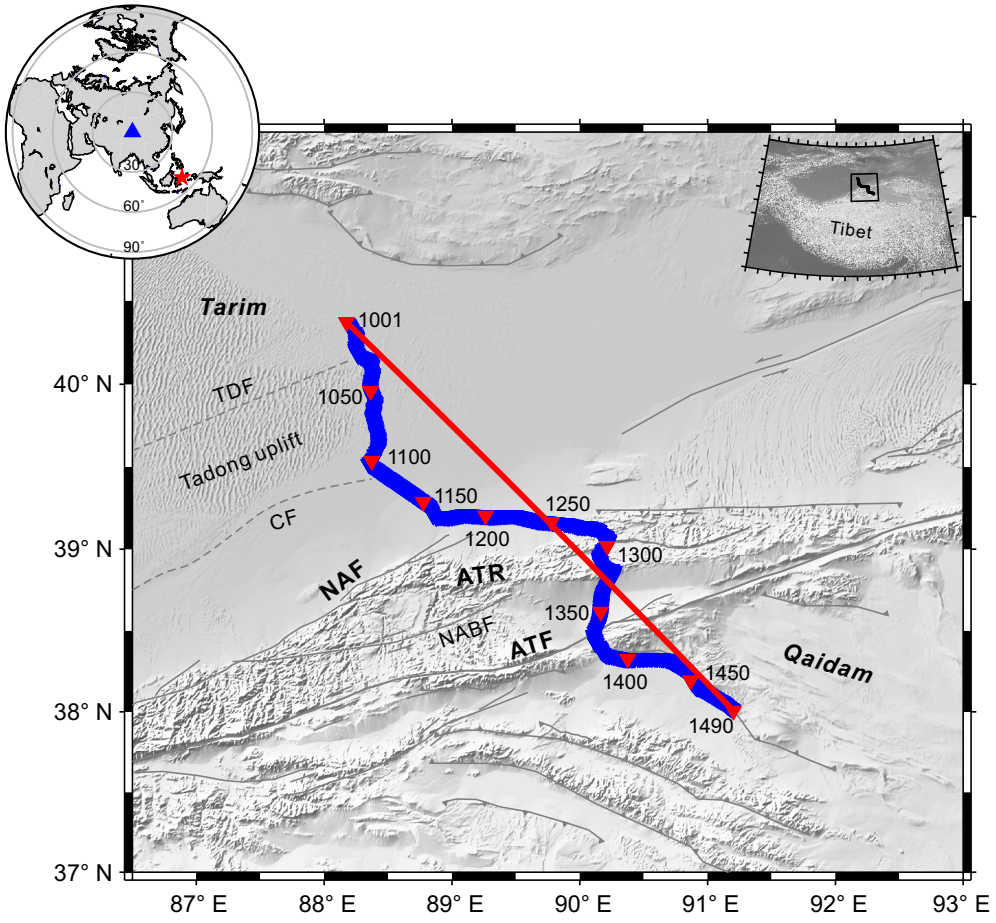

Figure 6. Simplified tectonic setting of the Altyn Tagh Range and location of the dense seismic array. The blue triangles denote the dense array with red ones annotated by numbers representing the station codes, and the blue line represents the linear imaging profile. The gray-solid lines denote the main faults, and the gray-dashed lines are nonreactivated faults. The top-left inset shows the earthquake event used to compute RFs for comparison, where the triangle and pentagram represent station and event, respectively. The top-right inset shows the surrounding tectonic units and the location of the dense array, where the black box and triangles represent the study region and seismic array, respectively. ATF, Altyn Tagh fault; ATR, Altyn Tagh Range; CF, Cherchen fault; NAF, North Altyn fault; NABF, North Altyn Brach fault; TDF, Tadong fault. The color version of this figure is available only in the electronic edition.

method. In this test, the duration of wavefield simulation is 85 s and the depth of the model is extended to 120 km. First, we simulate the teleseismic wavefield of this event using the presented velocity model (Fig. 7) and the developed hybrid method and recorded the wavefields at the same locations as the real stations. Figure 8 shows the observed and synthetic RFs profiles. It can be observed that the RFs are highly consistent between the observed and synthetic ones. Subsequently, we simulate wavefields from 10 events that are nearly parallel to the direction of the profile, and conduct common-converted-point (CCP) stacking using the same deconvolution algorithm (Ligorría and Ammon, 1999), migration technique, and parameters for the synthetic and observed RFs (Fig. 9). We refer readers to Wu *et al.* (2024) on real data processing and tectonic interpretation for details. It can be seen that we can successfully reproduce the real CCP image (Fig. 9b) based on synthetic RFs using the developed software package, which confirms the feasibility of the 2D hybrid method in RFs analysis on linear array.

Efficiency

This software package is a high programming optimized Fortran package supporting parallel computing using OpenMP (Chandra *et al.*, 2001). To demonstrate the efficiency of the 2D FD–FK hybrid method, all tests are run on the same laptop (four cores, Intel i7-4810MQ @ 2.8 GHz). We count the running time of the above tests. As shown in Figure 10, all tests just take a few minutes to several tens of minutes, which allows a large number of reproductive tests in real RFs applications. Compared to a 3D wavefield simulation, a 2D wavefield simulation code is very efficient and can significantly reduce computational time. Therefore, this software package frees one from computing exhaustive wavefield simulations to focus on verifying the reliability of the model through a large number of tests.

Discussions

Although this software package is efficient for high-frequency teleseismic wavefield modeling of RFs analysis, the amplitude of the radial component may be not accurate due to using 2D modeling code when the angle difference γ between the azimuth of the profile and the back azimuth of the event to station is too large. As the ratio of the transverse component to the total horizontal component is about $\sin^2\gamma = \frac{T}{\sqrt{R^2+T^2}}$, then the angle γ should be less than 18.4° if we set the amplitude error limit as 10%. Although the amplitude of the radial component may be not accurate for a large γ, its phase is still accurate. In real RFs analysis, this angle γ may be large. To completely circumvent this problem, one can select a subset of available events with small angle γ in reproductive tests to

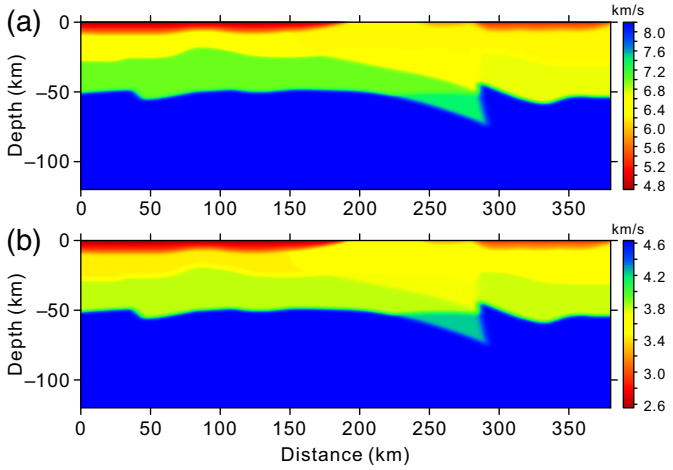

Figure 7. Velocity models of (a) V_P and (b) V_S along the dense seismic array across the Altyn Tagh Range. The color version of this figure is available only in the electronic edition.

verify the reliability of real CCP images just as done by Wu *et al.* (2024). In real data applications, we found that it is also applicable to cases when $\gamma > 18.4°$ but at the cost of weak spurious boundary diffractions. Therefore, this software package is a powerful and efficient tool for RFs analysis. Certainly, a hybrid method-based 3D teleseismic wavefield simulation software package may be more appealing for real applications. However, the computational cost will be increased exponentially, which prevents one from conducting a large number of reproductive tests for RFs analysis.

Conclusions

In this study, we developed a hybrid method that couples the FD and FK methods to simulate high-frequency teleseismic plane-wave propagation in 2D local media. It can take into account complex wave phenomena of the interactions between incoming teleseismic wavefields with local heterogeneities. This hybrid method can significantly reduce the computing cost of high-frequency teleseismic wavefield modeling, which is especially appealing for RFs analysis from distant earthquakes with thousands of kilometers. It is allowed to consider the real azimuthal effect of the source as the geographical locations of earthquakes are permitted. Comprehensive theoretical synthetic experiments demonstrate the effectiveness and accuracy of the developed method for *P*- and *S*-wave RFs analyses. The reproductive RFs profile for a real dataset further confirms the effectiveness and feasibility of the developed method. In terms of efficiency, this method just takes a few minutes to several tens of minutes to accomplish the simulation of the high-frequency teleseismic wavefield. Hence, this software package is a powerful tool for RFs analysis, which allows one to conduct a large number of numerical tests to verify the reliability of the RFs images and improve the velocity model accordingly.

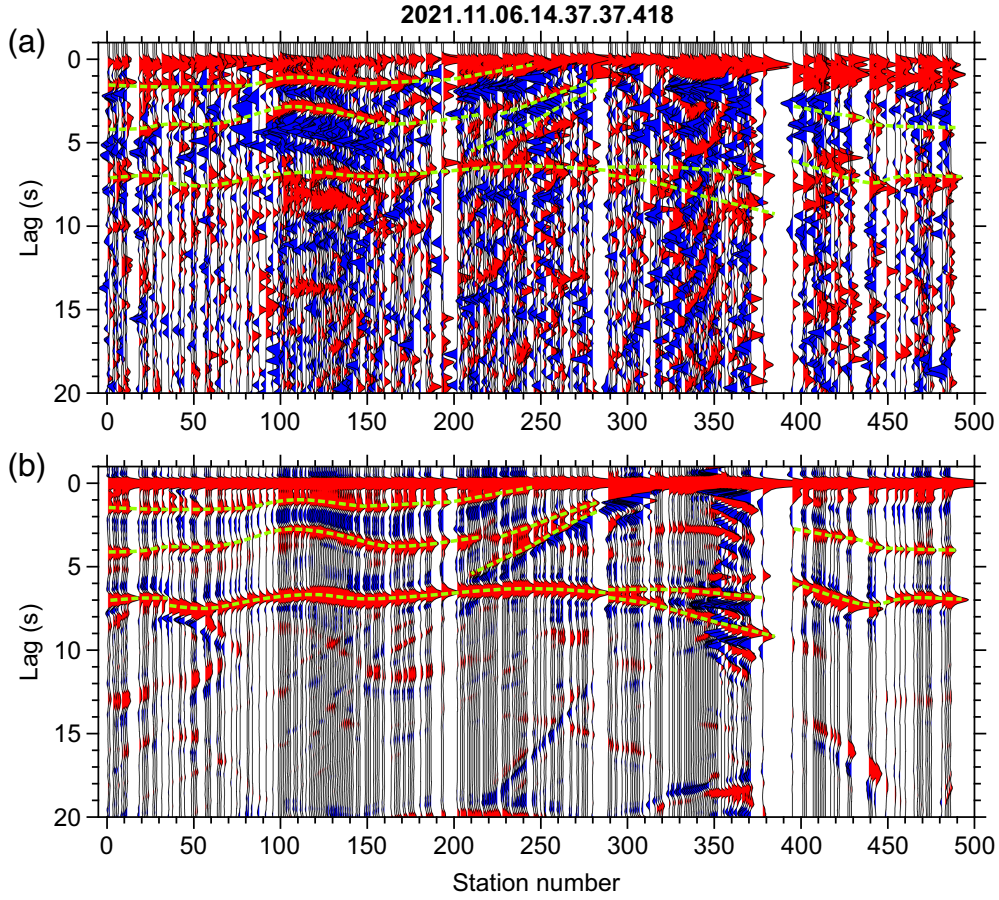

Figure 8. A comparison of (a) observed and (b) synthetic RFs profiles recorded from an earthquake is shown in Figure 6. The main phases are denoted by green-dashed lines. The color version of this figure is available only in the electronic edition.

Data and Resources

FDFK2D can be freely available at https://github.com/YoushanLiu/FDFK2D. The data used here as examples for receiver functions

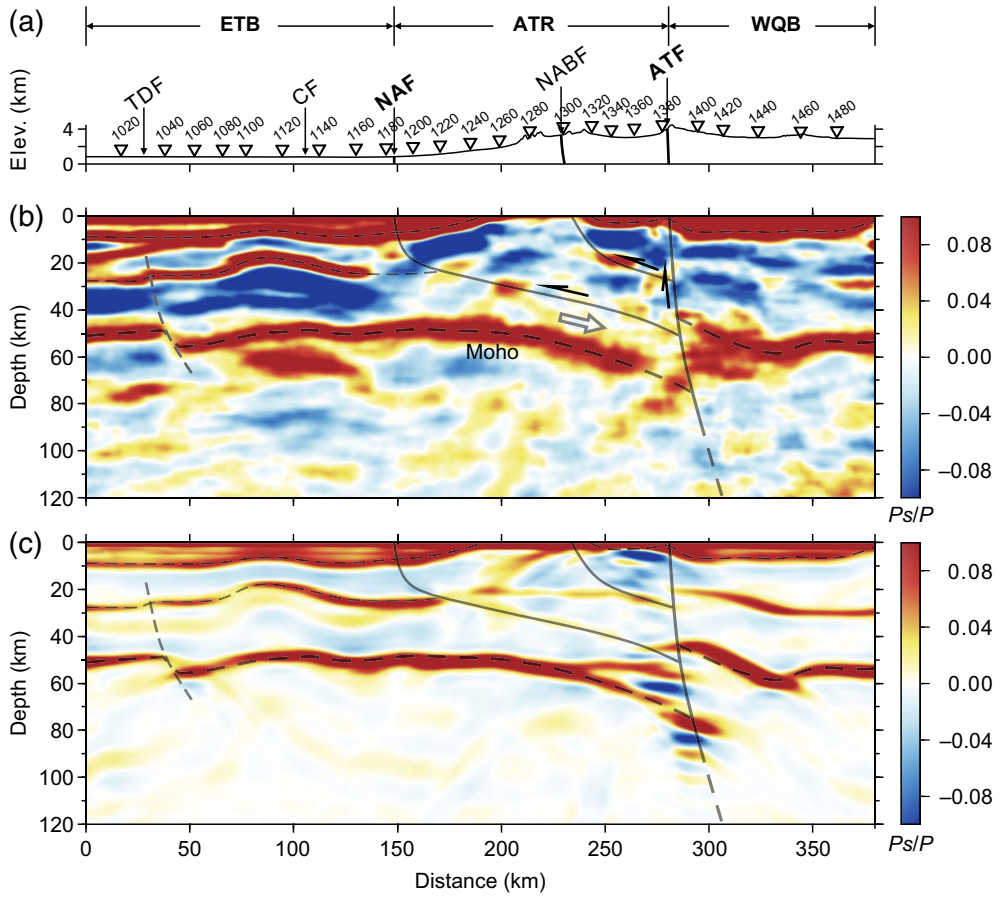

Figure 9. Comparison of the observed and synthetic common-converted-point (CCP) migrated images across the ATR. (a) Surface topography and stations along the profile. (b) Observed CCP image based on 41 distant earthquake events. (c) Synthetic CCP image based on inferred velocity model (Fig. 7) and synthetic RFs from 10 distant earthquake events almost parallel to the direction of the profile. Panels (b) and (c) are modified by Wu *et al.* (2024). The color version of this figure is available only in the electronic edition.

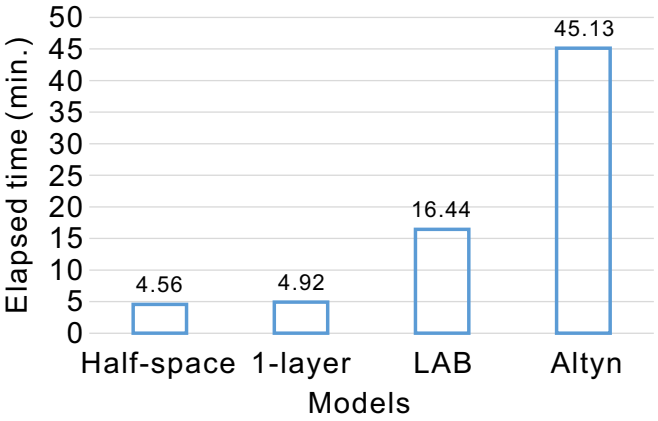

Figure 10. Histogram of elapsed time to compute seismograms for different models. The color version of this figure is available only in the electronic edition.

(RFs) calculation are released in software. Figures were plotted using Generic Mapping Tools (GMT) version 6 (Wessel *et al.*, 2019), which can be found at https://www.genericmapping-tools.org. The ray parameter of earthquake is computed by the *TauP* software (Crotwell *et al.*, 1999), which can be found at https://www.seis.sc.edu/taup. All websites were last accessed in November 2024.

Declaration of Competing Interests

The authors acknowledge that there are no conflicts of interest recorded.

Acknowledgments

The authors want to thank Editor-in-Chief Allison Bent, Associate Editor, and two anonymous reviewers for constructive suggestions, all of them contributed to substantially improve the early article and made possible a better presentation of this article. The authors are grateful for adapted with permission from Johm Wiley and Sons presented in Figure 9. Fruitful discussions with Professor Shaolin Liu are greatly appreciated. The authors gratefully acknowledge the financial support for this work contributed by the CAS Project for Young Scientists in Basic Research (YSBR-082), Second Tibetan Plateau Scientific Expedition and Research Program (STEP, 2019QZKK0701-02), the National Natural Science Foundation of China (Grant Numbers 41874065 and 42488201), and the Youth Innovation Promotion Association CAS (2023072).

References

Aki, K., and P. G. Richards (1980). *Quantitative Seismology*, Second Ed., W. H. Freeman and Co., San Francisco.

Alford, R. M., K. R. Kelly, and D. M. Boore (1974). Accuracy of finite-difference modeling of the acoustic wave equation, *Geophysics* **39,** no. 6, 834–842.

Alterman, Z., and F. C. Karal (1968). Propagation of elastic waves in layered media by finite difference methods, *Bull. Seismol. Soc. Am.* **58,** no. 1, 367–398.

Ammon, C. J. (1991). The isolation of receiver effects from teleseismic P waveforms, *Bull. Seismol. Soc. Am.* **81,** no. 6, 2504–2510.

Ba, Z., M. Wu, J. Liang, J. Zhao, and V. W. Lee (2022). A two-step approach combining FK with SE for simulating ground motion

due to point dislocation sources, *Soil Dynam. Earthq. Eng.* **157,** 107224, doi: 10.1016/j.soildyn.2022.107224.

Beller, S., V. Monteiller, S. Operto, G. Nolet, A. Paul, and L. Zhao (2018). Lithospheric architecture of the South-Western Alps revealed by multiparameter teleseismic full-waveform inversion, *Geophys. J. Int.* **212,** no. 2, 1369–1388.

Bielak, J., and P. Christiano (1984). On the effective seismic input for nonlinear soil-structure interaction systems, *Earthq. Eng. Struct. Dynam.* **12,** no. 1, 107–119.

Bielak, J., K. Loukakis, Y. Hisada, and C. Yoshimura (2003). Domain reduction method for three-dimensional earthquake modeling in localized regions, Part I: theory, *Bull. Seismol. Soc. Am.* **93,** no. 2, 817–824.

Brillouin, L. (1926). La mécanique ondulatoire de Schrödinger: une méthode générale de resolution par approximations successives, *Comptes Rendus de l'Académie des Sciences* **183,** 24–26.

Capdeville, Y., E. Chaljub, J. P. Vilotte, and J. P. Montagner (2003). Coupling the spectral element method with a modal solution for elastic wave propagation in global earth models, *Geophys. J. Int.* **152,** no. 1, 34–67.

Chandra, R., L. Dagum, D. Kohr, R. Menon, D. Maydan, and J. McDonald (2001). *Parallel Programming in OpenMP*, Morgan Kaufmann, San Diego.

Chen, L., C. Cheng, and Z. Wei (2009). Seismic evidence for significant lateral variations in lithospheric thickness beneath the central and western North China Craton, *Earth Planet. Sci. Lett.* **286,** nos. 1/2, 171–183.

Chen, L., M. Jiang, J. Yang, Z. Wei, C. Liu, and Y. Lin (2014). Presence of an intralithospheric discontinuity in the central and western North China Craton: Implications for destruction of the craton, *Geology* **42,** no. 3: 223–226.

Chevrot, S., V. Monteiller, D. Komatitsch, N. Fuji, and R. Martin (2011). A hybrid technique for 3-D waveform modeling and inversion of high frequency teleseismic body waves, in *Proc. of 2011 Eos Trans. AGU* (Fall Meet.), Abstract S11D-05.

Crotwell, H. P., T. J. Owens, and J. Ritsema (1999). The TauP Toolkit: Flexible seismic travel-time and ray-path utilities, *Seismol. Res. Lett.* **70,** 154–160.

Dablain, M. A. (1986). The application of high-order differencing to the scalar wave equation, *Geophysics* **51,** no. 2, 54–66.

Fäh, D., and P. Suhadolc (1994). Application of numerical wave-propagation techniques to study local soil effects: The case of benevento (Italy), *Pure Appl. Geophys.* **143,** no. 4, 513–536.

Fäh, D., P. Suhadolc, and G. F. Panza (1994). A hybrid method for the estimation of ground motion in sedimentary Basins: Quantitative modeling for Mexico city, *Bull. Seismol. Soc. Am.* **84,** no. 2, 383–399.

Farra, V., and L. Vinnik (2000). Upper mantle stratification by P and S receiver functions, *Geophys. J. Int.* **141,** no. 3, 699–712.

Fischer, K. M., H. A. Ford, D. L. Abt, and C. A. Rychert (2010). The lithosphere-asthenosphere boundary, *Annu. Rev. Earth Planet. Sci.* **38,** 551–575.

Galis, M., P. Moczo, and J. Kristek (2008). A 3-D hybrid finite-difference–finite-element viscoelastic modelling of seismic wave motion, *Geophys. J. Int.* **175,** no. 1, 153–184.

Haskell, N. B. (1953). The dispersion of surface waves on multilayered media, *Bull. Seismol. Soc. Am.* **43,** no. 1, 17–34.

Haskell, N. B. (1962). Crustal reflection of plane P and SV waves, *J. Geophys. Res.* **67,** no. 12, 4751–4767.

Huang, B. S., and R. C. Shih (1997). Numerical modeling for elastic wave propagation with a hybrid of the pseudo-spectrum and finite-element methods, *Terr. Atmos. Ocean. Sci.* **8,** no. 1, 1–12.

Jeffreys, H. (1924). On certain approximate solutions of linear differential equations of the second order, *Proc. Lond. Math. Soc.* **23,** 428–436.

Kelly, K. R., R. W. Ward, S. Treitel, and R. M. Alford (1976). Synthetic seismograms: A finite-difference approach, *Geophysics* **41,** no. 1, 2–27.

Komatitsch, D., and J. Tromp (1999). Introduction to the spectral element method for three-dimensional seismic wave propagation, *Geophys. J. Int.* **139,** no. 3, 806–822.

Komatitsch, D., S. Tsuboi, and J. Tromp (2005). The spectral-element method in seismology, in *Seismic Earth: Array Analysis of Broadband Seismograms*, A. Levander and G. Nolet (Editors), Geophysical Monograph, Vol. 157, 205–227, AGU, Washington.

Kramers, H. A. (1926). Wellenmechanik und halbzahlige Quantisierung, *Zeitschrift für Physik* **39,** no. 10–11, 828–840.

Lan, H., and Z. Zhang (2011). Comparative study of the free-surface boundary condition in two-dimensional finite-difference elastic wave field simulation, *J. Geophys. Eng.* **8,** no. 2, 275–286.

Langston, C. A. (1979). Structure under Mount Rainier, Washington, inferred from teleseismic body waves, *J. Geophys. Res.* **84**, no. B9, 4749–4762.

Leng, K., J. Korenaga, and T. Nissen-Meyer (2020). 3-D scattering of elastic waves by small-scale heterogeneities in the Earth's mantle, *Geophys. J. Int.* **223,** no. 1, 502–525.

Leng, K., T. Nissen-Meyer, and M. van Driel (2016). Efficient global wave propagation adapted to 3-D structural complexity: a pseudospectral/spectral-element approach, *Geophys. J. Int.* **207,** no. 3, 1700–1721.

Leng, K., T. Nissen-Meyer, M. van Driel, K. Hosseini, and D. Al-Attar (2019). AxiSEM3D: broad-band seismic wavefields in 3-D global earth models with undulating discontinuities, *Geophys. J. Int.* **217,** no. 3, 2125–2146.

Ligorría, J. P., and C. J. Ammon (1999). Iterative deconvolution and receiver-function estimation, *Bull. Seismol. Soc. Am.* **89,** no. 5, 1395–1400.

Liu, S., X. Li, W. Wang, and T. Zhu (2015). Source wavefield reconstruction using a linear combination of the boundary wavefield in reverse time migration, *Geophysics* **80,** no. 6, S203–S212.

Liu, S., D. Yang, X. Dong, Q. Liu, and Y. Zheng (2017). Element-by-element parallel spectral-element methods for 3-D teleseismic wave modeling, *Solid Earth* **8,** 969–986.

Liu, Y., J. Teng, H. Lan, X. Si, and X. Ma (2014). A comparative study of finite element and spectral element methods in seismic wavefield modeling, *Geophysics* **79,** no. 2, T91–T104.

Liu, Y., J. Teng, S. Liu, and D. Ma (2013). Explicit finite element method with triangle meshes stored by sparse format and its perfectly matched layers absorbing boundary condition, *Chinese J. Geophys.* **56,** no. 9, 3085–3099 (in Chinese).

Liu, Y., T. Xu, Y. Wang, J. Teng, J. Badal, and H. Lan (2019). An efficient source wavefield reconstruction scheme using single boundary layer values for the spectral element method, *Earth Planet. Phys.* **3,** no. 4, 342–357.

Lyu, C., L. Zhao, and Y. Capdeville (2022). Novel hybrid numerical simulation of the wave equation by combining physical and

numerical representation theorems and a review of hybrid methodologies, *J. Geophys. Res.* **127,** no. 5, e2021JB22368, doi: 10.1029/2021JB022368.

Ma, D., and G. Zhu (2004). Hybrid method combining finite element and pseudospectral method for solving the elastic wave equation, *J. Earth Sci. Environ.* 26**,** no. 1, 61–64 (in Chinese).

Ma, J., D. Yang, P. Tong, and X. Ma (2018). TSOS and TSOS-FK hybrid methods for modelling the propagation of seismic waves, *Geophys. J. Int.* **214,** no. 3, 1665–1682.

Ma, S., R. J. Archuleta, and P. Liu (2004). Hybrid modeling of elastic P-SV wave motion: A combined finite-element and staggered-grid finite-difference approach, *Bull. Seismol. Soc. Am.* **94,** no. 4, 1557–1563.

Mark, H. F., J. A. Collins, D. Lizarralde, G. Hirth, J. B. Gaherty, R. L. Evans, and M. D. Behn (2021). Constraints on the depth, thickness, and strength of the G discontinuity in the central pacific from s receiver functions, *J. Geophys. Res.* **126,** no. 4, e2019JB019256, doi: 10.1029/2019JB019256.

Meng, W., D. Yang, X. Dong, and J. Ma (2021). A 3D optimized frequency-wavenumber (FK), time-space optimized sympletic (TSOS) hybrid method for teleseismic wave modeling, *Bull. Seismol. Soc. Am.* **111,** no. 6, 3403–3419.

Moczo, P., E. Bystrický, J. Kristek, J. M. Carcione, and M. Bouchon (1997). Hybrid modeling of P-SV seismic motion at inhomogeneous viscoelastic topographic structures, *Bull. Seismol. Soc. Am.* **87,** no. 5, 1305–1323.

Moczo, P., J. Kristek, V. Vavryčuk, R. J. Archuleta, and L. Halada (2002). 3D heterogeneous staggered-grid finite-difference modeling of seismic motion with volume harmonic and arithmetic averaging of elastic moduli and densities, *Bull. Seismol. Soc. Am.* **92,** no. 8, 3042–2066.

Monteiller, V., S. Beller, B. Plazolles, and S. Chevrot (2020). On the validity of the planar wave approximation to compute synthetic seismograms of teleseismic body waves in a 3-D regional model, *Geophys. J. Int.* **224,** no. 3, 2060–2076.

Monteiller, V., S. Chevrot, D. Komatitsch, and N. Fuji (2013). A hybrid method to compute short-period synthetic seismograms of teleseismic body waves in a 3-D regional model, *Geophys. J. Int.* **192,** no. 1, 230–247.

Nábelek, J., G. György, J. Vergne, S. Sapkota, B. Kafle, M. Jiang, H. Su, J. John, B. S. Huang, and , and The HiClimb Team (2009). Underplating in the Himalaya-Tibet collision zone revealed by the Hi-CLIMB experiment, *Science* **325,** no. 5946, 1371–1374.

Nilsson, S., N. A. Petersson, B. Sjögreen, and H. O. Kreiss (2007). Stable difference approximations for the elastic wave equation in second order formulation,*SIAM J. Numer. Anal.* **45,** no. 5, 1902–1936.

Nissen-Meyer, T., M. van Driel, S. C. Stähler, K. Hosseini, S. Hempel, L. Auer, A. Colombi, and A. Fournier (2014). AxiSEM: Broadband 3-D seismic wavefields in axisymmetric media, *Solid Earth* **5,** no. 1, 425, doi: 10.5194/se-5-425-2014.

Opršal, I., and J. Zahradnik (2002). Three-dimensional finite difference method and hybrid modeling of earthquake ground motion, *J. Geophys. Res.* **107,** no. B8, ESE 2-1–ESE 2-16.

Opršal, I., B. J. Brokešová, D. Fäh, and D. Giardini (2002). 3D hybrid ray-FD and DWN-FD seismic modeling for simple models containing complex local structures, *Stud. Geophys. Geod.* **46,** 711–730.

Opršal, I., D. Fäh, P. M. Mai, and D. Giardini (2005). Deterministic earthquake scenario for the Basel area: Simulating strong motions and site effects for Basel, Switzerland, *J. Geophys. Res.* **110,** no. B4, doi: 10.1029/2004JB003188.

Robertsson, J. O. A., and C. H. Chapman (2000). An efficient method for calculating finite-difference seismograms after model alterations, *Geophysics* **65,** no. 3, 907–918.

Robertsson, J. O. A., A. Levander, and K. Holliger (1996). A hybrid wave propagation simulation technique for ocean acoustic problems, *J. Geophys. Res.* **101,** no. B5, 11,225–11,241.

Roecker, S., B. Baker, and J. McLaughlin (2010). A finite-difference algorithm for full waveform teleseismic tomography, *Geophys. J. Int.* **181,** no. 2, 1017–1040.

Rondenay, S. (2009). Upper mantle imaging with array recordings of converted and scattered teleseismic waves, *Surv. Geophys.* **30,** 377–405.

Shtivelman, V. (1984). A hybrid method for wave field computation, *Geophys. Propect.* **32,** no. 2, 236–257.

Shitivelman, V. (1985). Two-dimensional acoustic modeling by a hybrid method, *Geophysics* **50,** no. 8, 1273–1284.

Thomson, W. (1950). Transmission of elastic waves through a stratified solid medium, *J. Appl. Phys.* **21,** no. 89, 89–93.

Tong, P., C. W. Chen, D. Komatitsch, P. Basini, and Q. Liu (2014). High-resolution seismic imaging based on an SEM-FK hybrid method, *Geophys. J. Int.* **197,** no. 1, 369–395.

Tong, P., D. Komatitsch, T. L. Tseng, S. H. Hung, C. W. Chen, P. Basini, and Q. Liu (2014). A 3-D spectral-element and frequency-wave number hybrid method for high-resolution seismic array imaging, *Geophys. Res. Lett.* **41,** no. 20, 7025–7034.

Xu, M., K. Wang, J. Chen, D. Yu, and P. Tong (2024). Receiver function adjoint tomography for three-dimensional high-resolution seismic array imaging: Methodology and Applications in Southeastern Tibet, *Geophys. Res. Lett.* **50,** no. 19, e2023GL104077, doi: 10.1029/2023GL104077.

Yoshinmura, C., J. Bielak, Y. Hisada, and A. Fernández (2003). Domain reduction method for three-dimensional earthquake modeling in localized regions, Part II: Verification and applications, *Bull. Seismol. Soc. Am.* **93,** no. 2, 825–841.

Yuan, X. H., R. Kind, X. Li, and R. Wang (2006). The S receiver function: synthetics and data example, *Geophys. J. Int.* **165,** no. 2, 555–564.

van Manen, D. J., X. Li, M. Vasmel, F. Broggini, and J. Robertsson (2020). Exact extrapolation and immersive modelling with finite-difference injection, *Geophys. J. Int.* **223,** no. 1, 584–598.

Wang, B. L., and Z. H. Tian (2005). Application of finite element–finite difference method to the determination of transient temperature field in functionally graded materials, *Finite Elem. Anal. Des.* **41,** no. 4, 335–349.

Wen, L. X., and D. V. Helmberger (1998). A two-dimensional P-SV hybrid method and its application to modeling localized structures near the core-mantle boundary, *J. Geophys. Res.* **103,** no. B8, 17,901–17,918.

Wen, L. X., and Z. X. Yao (1994). Theory and application of hybrid method seismograms, *Acta Geophys. Sinica* **37,** no. 2, 211–219 (in Chinese).

Wen, L. X., and Z. X. Yao (1995). A study of the effects of the Feitsui canyon topography on the ground strong motion-using 2.5-D SH

hybrid method and the strong motion records at a station, *Acta Geophys. Sinica* **38,** no. 1, 64–70 (in Chinese).
Wentzel, G. (1926). Eine Verallgemeinerung der Quantenbedingungen für die Zwecke der Wellenmechanik, *Zeitschrift für Physik* **38,** no. 6–7, 518–529.
Wessel, P., J. F. Luis, L. Uieda, R. Scharroo, F. Wobbe, W. H. F. Smith, and D. Tian (2019). The Generic Mapping Tools Version 6, *Geochem. Geophys. Geosys.* **20,** no. 11, 5556–5564.
Wu, C., T. Xu, X. Tian, R. N. Mitchell, J. Lin, J. Yang, X. Wang, and Z. Lu (2024). Underthrusting of Tarim lower crust beneath the Tibetan plateau revealed by receiver function imaging, *Geophys. Res. Lett.* **51,** no. 2, e2024GL108220, doi: 10.1029/2024GL108220.
Wu, W., S. Ni, Z. Zhan, and S. Wei (2018). An SEM-DSM three-dimensional hybrid method for modelling teleseismic waves with complicated source-side structures, *Geophys. J. Int.* **215,** 133–154.
Zahradník, J., and P. Moczo (1996). Hybrid seismic modeling based on discrete-wave number and finite-difference methods, *Pure Appl. Geophys.* **148,** no. 1–2, 21–38.
Zhao, L., A. Paul, S. Guillot, S. Solarino, M. G. Malusà, T. Zheng, C. Aubert, S. Salimbeni, T. Dumont, S. Schwartz, *et al.* (2015). First seismic evidence for continental subduction beneath the Western Alps, *Geology* **43,** no. 9, 815–818.
Zhao, L., L. Wen, L. Chen, and T. Zheng (2008). A two-dimensional hybrid method for modeling seismic wave propagation in anisotropic media, *J. Geophys. Res.* **113,** no. B12, 307, doi: 10.1029/2008JB005733.
Zhao, L., M. Zhao, and G. Lu (2014), Upper mantle seismic anisotropy beneath a convergent boundary: SKS waveform modeling in central Tibet, *Sci. China Earth Sci.* **57,** 759–776.
Zhong, M., and Z. Zhan (2020). An array-based receiver function deconvolution method: methodology and application, *Geophys. J. Int.* **222,** no. 1, 1–14.
Zhu, L., and H. Kanamori (2000). Moho depth variation in southern California from teleseismic receiver functions, *J. Geophys. Res.* **105,** no. B2, 2969–2980.
Zhu, L., and L. A. Rivera (2002). A note on the dynamic and static displacements from a point source in multilayered media, *Geophys. J. Int.* **148,** no. 3, 619–627.

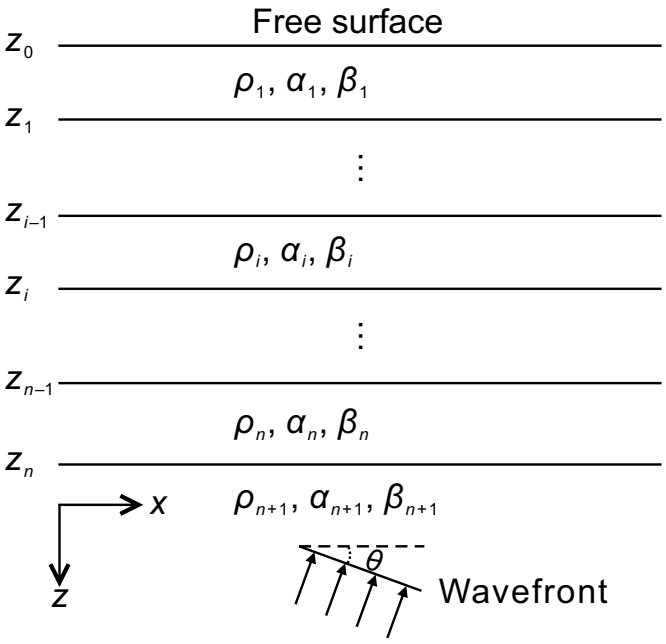

Figure A1. An *n*-layer over the half-space model. The depth of the top boundary of *i*th layer is denoted by z_i, density, V_P, and V_S, which are represented by ρ_i, α_i, and β_i, respectively. A teleseismic plane wavefront with an incidence angle of θ is initialized at the reference point (x_o, z_o). The positive directions of the *x*- and *z*-axes are rightward and downward, respectively.

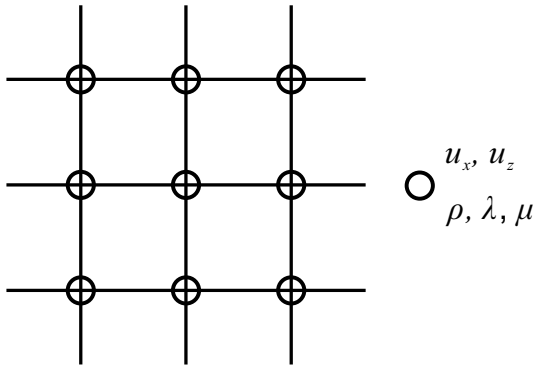

Figure A2. Schematic diagram of finite-difference (FD) stencil. The wavefields and material parameters are defined at regular collocated grids.

Appendix A

Frequency–wavenumber (FK) method for *P–SV* wave in 1D layered models

The first-order displacement–stress wave equations in 3D isotropic media take the following forms (Aki and Richards, 1980):

$$\rho u_i = \sigma_{ij,j} + f_i, \tag{A1}$$

in which subscript i takes x, y, or z; u_i is the ith displacement component that is a function of time t and space coordinate (x, y, z); ρ is mass density; $\sigma_{ij} = c_{ijkl}\varepsilon_{kl}$ is the stress tensor; $\varepsilon_{ij} = \frac{1}{2}(u_{i,j} + u_{j,i})$ is the strain tensor; c_{ijkl} is the elastic coefficient tensor in isotropic media that is $c_{ijkl} = \lambda\delta_{ij}\delta_{kl} + \mu(\delta_{ik}\delta_{jl} + \delta_{il}\delta_{jk})$; λ and μ are Lamé constants; f is the source term.

Transforming the wave equation (A1) with respect to (t, x, y) into the (ω, k_x, k_y) domain, we obtain the following equations (Liu *et al.*, 2017):

$$-\rho\omega^2 \begin{bmatrix} u_x^{\mathrm{FK}} \\ u_y^{\mathrm{FK}} \\ u_z^{\mathrm{FK}} \end{bmatrix} = \begin{bmatrix} ik_x\sigma_{xx} + ik_y\sigma_{xy} + \partial_z\sigma_{xz} \\ ik_x\sigma_{xy} + ik_y\sigma_{yy} + \partial_z\sigma_{yz} \\ ik_x\sigma_{xz} + ik_y\sigma_{yz} + \partial_z\sigma_{zz} \end{bmatrix}, \tag{A2}$$

in which $\mathbf{u}^{\mathrm{FK}} = (u_x^{\mathrm{FK}}, u_y^{\mathrm{FK}}, u_z^{\mathrm{FK}})$ is the displacement of plane-wave solution in the frequency domain and layered model;

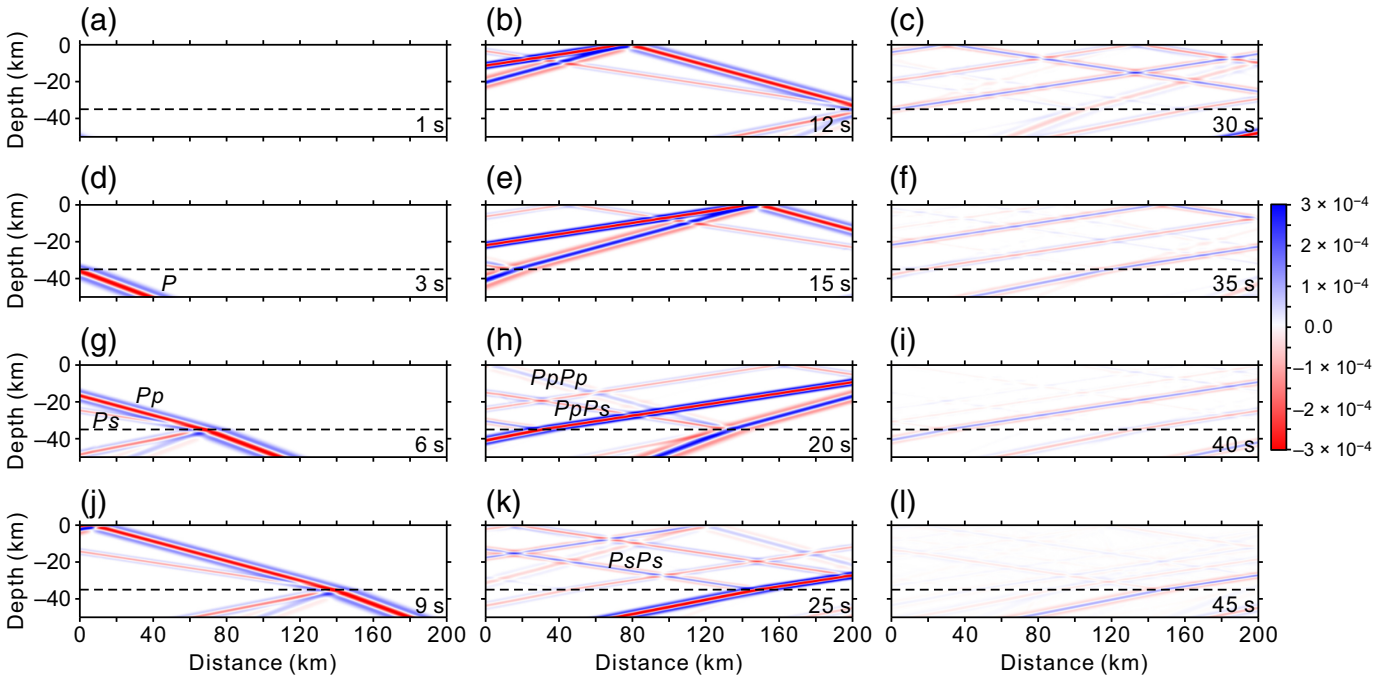

Figure A3. Snapshots of horizontal displacement components of incident *P* wave computed by the FD–frequency–wavenumber (FK) hybrid method in a single-layer over half-space model are shown in Panels (a–l). Numbers at right-bottom corners are corresponding time instants. Phases *P*, *Pp*, and *Ps* denote the direct *P* wave, transmitted *P* wave, and converted *S* wave, whereas phases *PpPp*, and *PpPs* are corresponding multiples, respectively. The color version of this figure is available only in the electronic edition.

σ_{xx}, σ_{yy}, σ_{zz}, σ_{yz}, σ_{xz}, and σ_{xy} are the components of the stress tensor in the frequency domain; k_x and k_y are the wavenumbers in the x and y directions, respectively; ω is angular frequency; i is the imaginary number. Here, we use the same symbol in both the time–space and frequency–wavenumber domains to avoid clustering. If we define $u_{\mathrm{FK}}\mathbf{e}_h = u_x\mathbf{e}_x + u_y\mathbf{e}_y$ and $k_h\mathbf{e}_h = k_x\mathbf{e}_x + k_y\mathbf{e}_y$, in which $k_h = \sqrt{k_x^2 + k_y^2}$ and $\mathbf{e}_h$ is the horizontal unit normal vector, then equation (A2) can be written (Liu *et al.*, 2017)

$$-\rho\omega^2\begin{bmatrix} u_x^{\mathrm{FK}} \\ u_z^{\mathrm{FK}} \end{bmatrix} = \begin{bmatrix} ik_h\sigma_{xh} + \partial_z\sigma_{zz} \\ ik_h\sigma_{hz} + \partial_z\sigma_{zz} \end{bmatrix}. \tag{A3}$$

Thus, $u_x = u_{\mathrm{FK}}\cos\phi$, $u_y = u_{\mathrm{FK}}\sin\phi$ in which ϕ is the back-azimuth angle between station and source. Then equation (A3) can be organized as following ordinary equation:

$$\frac{d}{dz}\begin{bmatrix} y_1 \\ y_2 \\ y_3 \\ y_4 \end{bmatrix} = \begin{bmatrix} 0 & -ik_h & \frac{1}{\mu} & 0 \\ -\frac{ik_h\lambda}{\lambda+2\mu} & 0 & 0 & \frac{1}{\lambda+2\mu} \\ \frac{4k_h^2\mu(\lambda+\mu)}{\lambda+2\mu} - \rho\omega^2 & 0 & 0 & -\frac{ik_h\lambda}{\lambda+2\mu} \\ 0 & -\rho\omega^2 & -ik_h & 0 \end{bmatrix}\begin{bmatrix} y_1 \\ y_2 \\ y_3 \\ y_4 \end{bmatrix} = \mathbf{E}\mathbf{y}, \tag{A4}$$

in which $y_1 = u_x^{\mathrm{FK}}$, $y_2 = u_z^{\mathrm{FK}}$, $y_3 = \sigma_{hz}$, and $y_4 = \sigma_{zz}$. By computing the eigenvalues and eigenvectors of the matrix $\mathbf{E} = \mathbf{RDR}^{-1}$, the general solution of ordinary equation (A4) can be obtained:

$$\begin{aligned} y &= \begin{bmatrix} \frac{k_z^s}{k_h} & -\frac{k_z^s}{k_h} & 1 & 1 \\ 1 & 1 & -\frac{k_z^p}{k_h} & \frac{k_z^p}{k_h} \\ -i\frac{\mu\gamma}{k_h} & -i\frac{\mu\gamma}{k_h} & -2i\mu k_z^p & 2i\mu k_z^p \\ -2i\mu k_z^s & 2i\mu k_z^s & i\frac{\mu\gamma}{k_h} & i\frac{\mu\gamma}{k_h} \end{bmatrix} \\ &= \begin{bmatrix} e^{-ik_z^s z} & 0 & 0 & 0 \\ 0 & e^{ik_z^s z} & 0 & 0 \\ 0 & 0 & e^{-ik_z^p z} & 0 \\ 0 & 0 & 0 & e^{ik_z^p z} \end{bmatrix}\begin{bmatrix} D_S \\ U_S \\ D_P \\ U_P \end{bmatrix}, \end{aligned} \tag{A5}$$

in which each column of the matrix $\mathbf{R}$ is the eigenvector of the matrix $\mathbf{E}$; the diagonal elements of the matrix $\mathbf{D}$ are the eigenvalues of the matrix $\mathbf{E}$; $\alpha = \sqrt{\frac{\lambda+2\mu}{\rho}}$ and $\beta = \sqrt{\frac{\mu}{\rho}}$ are the seismic velocities of P and S waves, respectively; $k_z^p = \sqrt{\frac{\omega^2}{\alpha^2} - k_h^2}$, $k_z^s = \sqrt{\frac{\omega^2}{\beta^2} - k_h^2}$, and $\gamma = \frac{\omega^2}{\beta^2} - 2k_h^2$. As the positive direction of the z-axis is downward, the coefficients D_S, U_S, D_P, and U_P are amplitudes of the downgoing S wave, upgoing S wave, downgoing P wave, and upgoing P wave, respectively. For any invertible diagonal matrix $\mathbf{S}$, $\mathbf{SDS}^{-1} = \mathbf{D}$ as $\mathbf{D}$ is a diagonal matrix. Thus, for $\mathbf{V} = \mathbf{RS}$, $\mathbf{VDV}^{-1} = \mathbf{RSDS}^{-1}\mathbf{R}^{-1} = \mathbf{RDR}^{-1} = \mathbf{E}$. Therefore, the eigenvector matrix $\mathbf{R}$ is nonunique as it is equivalent to right multiplying itself by any invertible diagonal matrix $\mathbf{S}$.

For the layered model as shown in Figure A1, we can obtain the following recursive relationship of wavefields between $z = z_{i-1}$ and $z = z_i$ layers by using the equation (A5) and the continuous boundary conditions of displacements and normal stresses:

$$\mathbf{y}_{i-1} = \mathbf{P}_i \mathbf{y}_i, \tag{A6}$$

$$\mathbf{R}_i = \begin{bmatrix} \frac{k_z^s}{k_h} & -\frac{k_z^s}{k_h} & 1 & 1 \\ 1 & 1 & -\frac{k_z^p}{k_h} & \frac{k_z^p}{k_h} \\ -i\frac{\mu_i \gamma_i}{k_h} & -i\frac{\mu_i \gamma_i}{k_h} & -2i\mu_i k_z^p & 2i\mu_i k_z^p \\ -2i\mu_i k_z^s & 2i\mu_i k_z^s & i\frac{\mu_i \gamma_i}{k_h} & i\frac{\mu_i \gamma}{k_h} \end{bmatrix}, \tag{A7}$$

$$\mathbf{H}(z_{i-1} - z_i) = \begin{bmatrix} e^{-ik_z^s(z_{i-1}-z_i)} & 0 & 0 & 0 \\ 0 & e^{ik_z^s(z_{i-1}-z_i)} & 0 & 0 \\ 0 & 0 & e^{-ik_z^p(z_{i-1}-z_i)} & 0 \\ 0 & 0 & 0 & e^{ik_z^p(z_{i-1}-z_i)} \end{bmatrix}, \tag{A8}$$

in which μ_i and γ_i are the corresponding variables in the ith layer, respectively. Here, we define what is called propagation matrix, which establishes the relationship of the displacement and normal stress components between the $i-1$th and ith layers. Hence, the FK method is also called the propagator matrix method. Using the equations (A5) and (A6), we can obtain the wavefield on the free-surface responses to the plane wave initialized at location (x_o, y_o, z_o):

$$\mathbf{y}_{z=z_0} = \mathbf{P}_1 \mathbf{P}_2 \cdots \mathbf{P}_n \mathbf{R}_{n+1} \mathbf{H}(z_n - z_o) \begin{bmatrix} D_S \\ U_S \\ D_P \\ U_P \end{bmatrix} e^{-ik_h[(x-x_o)\cos\phi + (y-y_o)\sin\phi]}. \tag{A9}$$

We define the propagator matrix of n-layer model as

$$\mathbf{A} = \mathbf{P}_1 \mathbf{P}_2 \cdots \mathbf{P}_n \mathbf{R}_{n+1} \mathbf{H}(z_n - z_o) e^{-ik_h[(x-x_o)\cos\phi + (y-y_o)\sin\phi]} = \begin{bmatrix} a_{11} & a_{12} & a_{13} & a_{14} \\ a_{21} & a_{22} & a_{23} & a_{24} \\ a_{31} & a_{32} & a_{33} & a_{34} \\ a_{41} & a_{42} & a_{43} & a_{44} \end{bmatrix}. \tag{A10}$$

P-wave incidence

For the incident P wave, $U_S = 0$, $k_h = \frac{\omega}{\alpha} sin\theta$, in which θ is the incident angle of the plane wave. Applying the free-surface boundary condition, we can obtain the following equations for P-wave incidence:

$$\begin{bmatrix} 0 \\ 0 \end{bmatrix} = \begin{bmatrix} a_{31} & a_{32} & a_{33} & a_{34} \\ a_{41} & a_{42} & a_{43} & a_{44} \end{bmatrix} \begin{bmatrix} D_S \\ 0 \\ D_P \\ U_P \end{bmatrix}. \tag{A11}$$

Thus, we can obtain the unknown downgoing amplitudes of P and S waves in $n + 1$th layer:

$$\begin{bmatrix} D_S \\ D_P \end{bmatrix} = -\frac{1}{a_{31}a_{43} - a_{41}a_{33}} \begin{bmatrix} a_{43} & -a_{33} \\ -a_{41} & a_{31} \end{bmatrix} \begin{bmatrix} a_{34} \\ a_{44} \end{bmatrix} U_P. \tag{A12}$$

If the incident P wave has unit amplitude, its displacement response to the half-space model is $\mathbf{u} = (\sin\theta, \cos\theta)$. Using the equation (A5), we can obtain the free-surface displacement response to the unit amplitude of the incident P wave:

$$\begin{bmatrix} u_x^{FK} \\ u_z^{FK} \end{bmatrix} = \begin{bmatrix} -\frac{k_z^s}{k_h} & 1 \\ 1 & \frac{k_z^p}{k_h} \end{bmatrix} \begin{bmatrix} 0 \\ U_P \end{bmatrix} = \begin{bmatrix} \sin\theta \\ \cos\theta \end{bmatrix}, \tag{A13}$$

that is, $U_P = \pm \sin\theta$.

S-wave incidence

For the incident S wave, $U_P = 0$, $k_h = \frac{\omega}{\beta} sin\theta$. Applying the free-surface boundary condition, we can obtain the following equations for S-wave incidence:

$$\begin{bmatrix} 0 \\ 0 \end{bmatrix} = \begin{bmatrix} a_{31} & a_{32} & a_{33} & a_{34} \\ a_{41} & a_{42} & a_{43} & a_{44} \end{bmatrix} \begin{bmatrix} D_S \\ U_S \\ D_P \\ 0 \end{bmatrix}. \tag{A14}$$

Then we can obtain the unknown downgoing amplitudes of P and S waves in $n + 1$th layer:

$$\begin{bmatrix} D_S \\ D_P \end{bmatrix} = -\frac{1}{a_{31}a_{43} - a_{41}a_{33}} \begin{bmatrix} a_{43} & -a_{33} \\ -a_{41} & a_{31} \end{bmatrix} \begin{bmatrix} a_{32} \\ a_{42} \end{bmatrix} U_S. \tag{A15}$$

In this case, the free-surface displacement response to the unit amplitude of the S wave is $\mathbf{u} = (\cos\theta, \sin\theta)$. Using the equation (A5), we can obtain the free-surface displacement response to the unit amplitude of the incident S wave:

$$\begin{bmatrix} u_x^{FK} \\ u_z^{FK} \end{bmatrix} = \begin{bmatrix} -\frac{k_z^s}{k_h} & 1 \\ 1 & \frac{k_z^p}{k_h} \end{bmatrix} \begin{bmatrix} U_S \\ 0 \end{bmatrix} = \begin{bmatrix} \cos\theta \\ \sin\theta \end{bmatrix}, \tag{A16}$$

that is, $U_S = \pm \sin\theta$.

Wavefield downward continuation

For wavefields at a location beneath the surface, such as located at (x_r, y_r, z_r) in ith layer, we can obtain corresponding wavefields using the following recursive relationship:

$$\mathbf{y}_{z=z_r} = \mathbf{R}_i \mathbf{H}(z_r - z_{i-1}) \mathbf{R}_i^{-1} \mathbf{P}_{i-1}^{-1} \cdots \mathbf{P}_2^{-1} \mathbf{P}_1^{-1} \mathbf{y}_{z=z_0}. \tag{A17}$$

Appendix B

Discretization of finite-difference (FD) method

Discretization of the first-order derivative. In formula (3), the first-order derivatives are involved, which can be discretized as follows:

$$\frac{\partial u^n_{i+k-1/2,j}}{\partial x} \approx \sum_{m=1}^{N} c^N_m \frac{u^n_{i+k+m-1,j} - u^n_{i+k-m,j}}{\Delta x}, \tag{B1}$$

$$\frac{\partial u^n_{i+k,j}}{\partial z} \approx \sum_{m=1}^{N} d^N_m \frac{u^n_{i+k+m,j} - u^n_{i+k-m,j}}{2\Delta z}. \tag{B2}$$

Discretization of mixed derivatives in the coupling domain. To discretize the formula (4b) with second-order precision FD operator, the mixed derivative at node A can be approximated as

$$\begin{aligned}\frac{\partial}{\partial x}\left[M\frac{\partial u^n_{c_{i,j}}}{\partial z}\right]_A &\approx \frac{M_{i+1,j}(u^n_{c_{i+1,j+1}} - u^n_{c_{i+1,j-1}}) - M_{i-1,j}(u^n_{c_{i-1,j+1}} - u^n_{c_{i-1,j-1}})}{4\Delta x\Delta z} \\ &\approx \frac{M_{i+1,j}(u^n_{\mathrm{hy}_{i+1,j+1}} - u^n_{\mathrm{hy}_{i+1,j-1}}) - M_{i-1,j}(u^n_{\mathrm{hy}_{i-1,j+1}} - u^n_{\mathrm{hy}_{i-1,j-1}}) - M_{i-1,j}(u^n_{0_{i-1,j+1}} - u^n_{0_{i-1,j-1}})}{4\Delta x\Delta z},\end{aligned} \tag{B3}$$

while the mixed derivative at node B can be approximated as

$$\begin{aligned}\frac{\partial}{\partial x}\left[M\frac{\partial u^n_{s_{i,j}}}{\partial z}\right]_B &\approx \frac{M_{i+1,j}(u^n_{s_{i+1,j+1}} - u^n_{s_{i+1,j-1}}) - M_{i-1,j}(u^n_{s_{i-1,j+1}} - u^n_{s_{i-1,j-1}})}{4\Delta x\Delta z} \\ &\approx \frac{M_{i+1,j}(u^n_{hy_{i+1,j+1}} - u^n_{hy_{i+1,j-1}}) - M_{i-1,j}(u^n_{hy_{i-1,j+1}} - u^n_{hy_{i-1,j-1}}) - M_{i+1,j}(u^n_{0_{i+1,j+1}} - u^n_{0_{i+1,j-1}})}{4\Delta x\Delta z}.\end{aligned} \tag{B4}$$

Discretization of density and elastic modulus. As shown in Figure A2, the wavefields, density, and elastic moduli are defined at regular nodes, whereas the elastic moduli at half-grid nodes are involved in formulas (7a) and (7b). Using the boundary conditions of strain discontinuity and stress continuity at the interface, the material parameters not at grid nodes are approximated as (Moczo *et al.*, 2002)

$$\rho_{i,j} = \frac{1}{\Delta x\Delta y}\int_{x_{i-1/2}}^{x_{i+1/2}}\int_{y_{j-1/2}}^{y_{j+1/2}} \rho dxdy, \tag{B5}$$

$$M_{i+1/2,j} = \left(\frac{1}{\Delta x\Delta y}\int_{x_i}^{x_{i+1}}\int_{y_{j-1/2}}^{y_{j+1/2}} \frac{1}{M} dxdy\right)^{-1}. \tag{B6}$$

Manuscript received 31 May 2024
Published online 18 December 2024